Article

Cell

Glia Accumulate Evidence that Actions Are Futile and Suppress Unsuccessful Behavior

Graphical Abstract

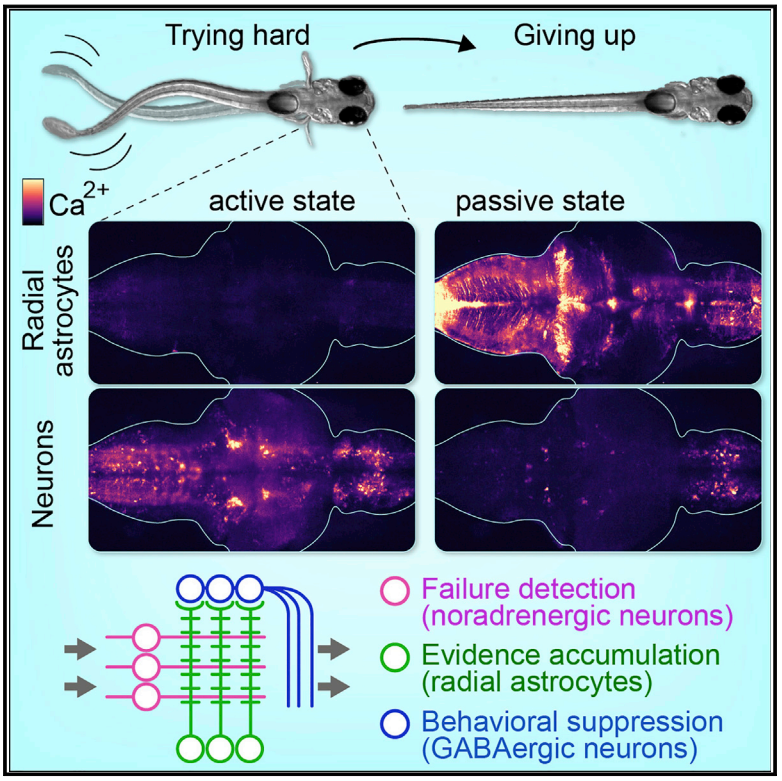

Authors

Yu Mu, Davis V. Bennett, Mikail Rubinov, ..., Brett D. Mensh, Loren L. Looger, Misha B. Ahrens

Correspondence

muy@janelia.hhmi.org (Y.M.), ahrensm@janelia.hhmi.org (M.B.A.)

In Brief

Whole-brain imaging in virtual-reality-immersed zebrafish reveals that failed swim attempts are detected by noradrenergic neurons, which drive glial cells that accumulate calcium until they trigger the suppression of further futile attempts.

Highlights

- Zebrafish "give up" after swim attempts repeatedly fail to generate movement
- Whole-brain imaging reveals noradrenergic neurons that encode swim failures
- Radial astrocytes accumulate the noradrenergic failure signal and trigger passivity
- Glia accumulate evidence that actions are futile, then switch behavioral state

Mu et al., 2019, Cell *178*, 27–43
June 27, 2019
https://doi.org/10.1016/j.cell.2019.05.050

CellPress

Cell

Glia Accumulate Evidence that Actions Are Futile and Suppress Unsuccessful Behavior

Yu Mu,[1,4,*] Davis V. Bennett,[1,2,4] Mikail Rubinov,[1,3,4] Sujatha Narayan,[1] Chao-Tsung Yang,[1] Masashi Tanimoto,[1] Brett D. Mensh,[1] Loren L. Looger,[1] and Misha B. Ahrens[1,5,*]
[1]Janelia Research Campus, Howard Hughes Medical Institute, Ashburn, VA, USA
[2]Department of Organismal Biology and Anatomy, University of Chicago, Chicago, IL, USA
[3]Department of Biomedical Engineering, Vanderbilt University, Nashville, TN, USA
[4]These authors contributed equally
[5]Lead Contact
*Correspondence: muy@janelia.hhmi.org (Y.M.), ahrensm@janelia.hhmi.org (M.B.A.)
https://doi.org/10.1016/j.cell.2019.05.050

SUMMARY

When a behavior repeatedly fails to achieve its goal, animals often give up and become passive, which can be strategic for preserving energy or regrouping between attempts. It is unknown how the brain identifies behavioral failures and mediates this behavioral-state switch. In larval zebrafish swimming in virtual reality, visual feedback can be withheld so that swim attempts fail to trigger expected visual flow. After tens of seconds of such motor futility, animals became passive for similar durations. Whole-brain calcium imaging revealed noradrenergic neurons that responded specifically to failed swim attempts and radial astrocytes whose calcium levels accumulated with increasing numbers of failed attempts. Using cell ablation and optogenetic or chemogenetic activation, we found that noradrenergic neurons progressively activated brainstem radial astrocytes, which then suppressed swimming. Thus, radial astrocytes perform a computation critical for behavior: they accumulate evidence that current actions are ineffective and consequently drive changes in behavioral states.

INTRODUCTION

Perseverance can lead to success, but some challenges are best met by high-activity bursts separated by behavioral quiescence. This pattern is often seen in motile animals that find themselves unable to move. Captured prey may become passive while waiting for a predator to loosen its grip before trying hard to escape; a fish stuck in mud may conserve energy between vigorous attempts to free itself. Periods of passivity are also observed during laboratory tasks in which an animal's actions fail to overcome challenges (e.g., passive coping, learned helplessness) (Andalman et al., 2019; Maier, 1984; Warden et al., 2012) or fail to acquire rewards (Salamone et al., 2016). Here, we studied the mechanisms of a form of "futility-induced passivity" in zebrafish to ask: how does the brain detect failures, accumulate evidence over time to infer that its motor patterns (attempts) are futile, and switch behavioral strategy?

To search for neurons involved in behavioral-state switching, we used whole-brain light-sheet imaging to survey single-cell dynamics during behavior in larval zebrafish. Because astrocytes influence neuronal activity (Bazargani and Attwell, 2016; Nedergaard, 1994; Parpura et al., 1994), we also imaged a glial cell type in zebrafish we refer to as radial astrocytes (a cell type previously also referred to in zebrafish as radial astroglia, astroglia, radial glia) (Cuoghi and Mola, 2009; Grupp et al., 2010). These cells have an apical-basal projection and bushy processes, similar to mammalian radial glia and astrocytes, respectively (Lyons and Talbot, 2014).

Interactions between astrocytes and neurons have been investigated extensively. Astrocytes can respond to neuronal activity by intracellular calcium increase. They can, in turn, influence other neurons through multiple mechanisms (Bazargani and Attwell, 2016), such as transmitter release (Araque et al., 2014) or modulation of extracellular potassium concentration (Haydon and Nedergaard, 2014; Wang et al., 2015). They play a role in controlling the states of neural networks, perform spatial and temporal integration, and can underlie slow shifts in brain states (Araque et al., 2014) like sleep and seizures (Kjaerby et al., 2017; Verdugo et al., 2019). Calcium signals in astrocytes are triggered by sensory input and behavior (Bekar et al., 2008; Ma et al., 2016; Paukert et al., 2014; Schummers et al., 2008; Srinivasan et al., 2015; Verkhratsky et al., 1998). Astrocytes can modulate circuit function and behavior (Cui et al., 2018; Gourine et al., 2010; Morquette et al., 2015; Yu et al., 2018). They can enhance memories (Adamsky et al., 2018), integrate neuronal signals over time (Deemyad et al., 2018), respond to neuromodulators including norepinephrine (NE) (Bekar et al., 2008; Ma et al., 2016; Paukert et al., 2014; Srinivasan et al., 2015; Verkhratsky et al., 1998), and serve as intermediaries between neuromodulators and neurons (Ma et al., 2016; Pabst et al., 2016). These findings raise the possibility that astrocytes play further roles typically ascribed to neurons, such as driving rapid behavioral-state switches.

To investigate brain-wide neuronal and astrocytic activity during futility-induced passivity, we used a virtual-reality (VR) environment to first simulate realistic visual feedback during attempted swimming; we then suddenly withheld this feedback to

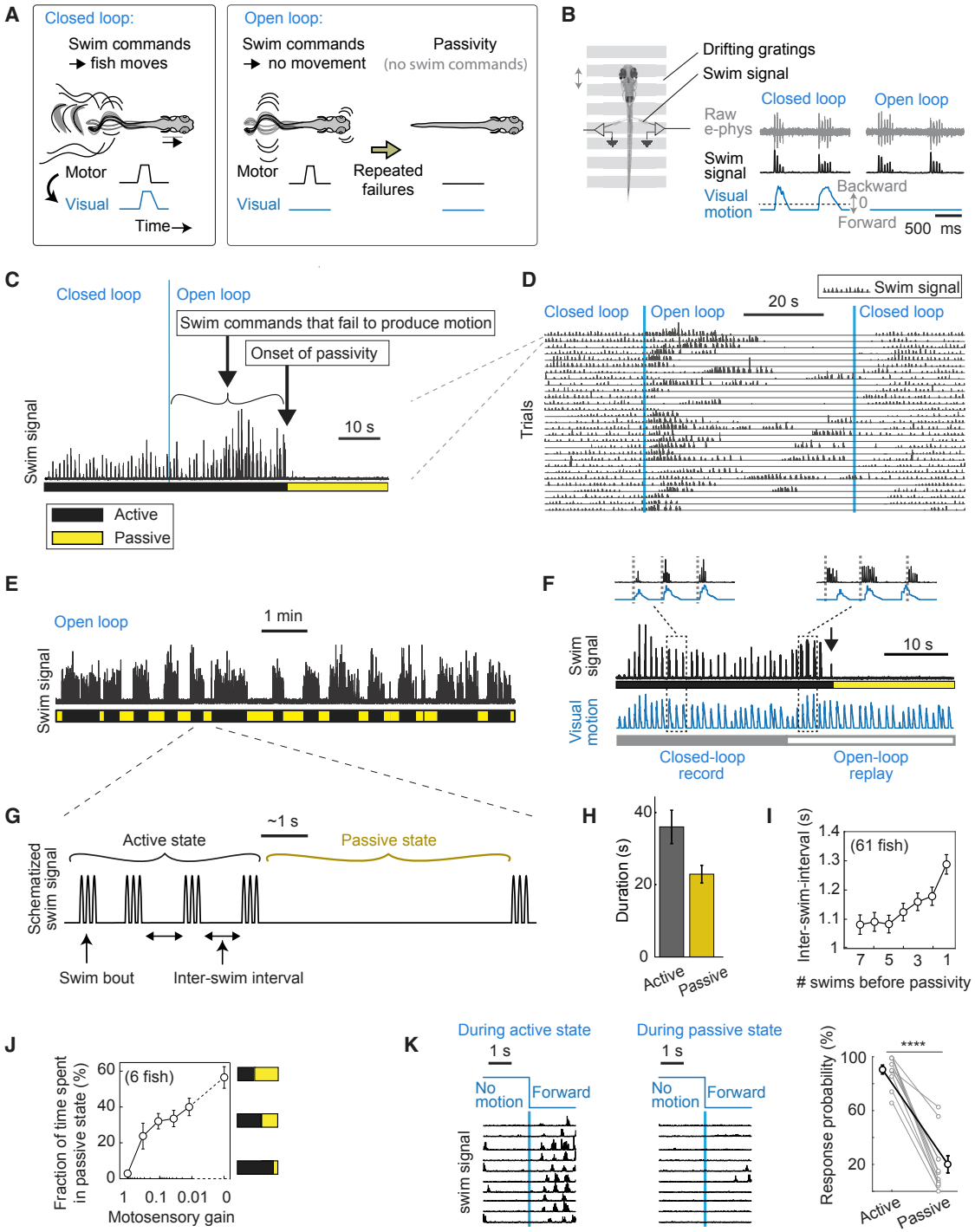

Figure 1. Lack of Visual Feedback during Swimming Triggers Passive Behavioral State

Figure360▷ For a Figure360 author presentation of this figure, see https://doi.org/10.1016/j.cell.2019.05.050.

(A) Locomotion in closed loop versus open loop. After repeated swim failures, zebrafish entered a passive behavioral state.

(B) Virtual environment for fictively swimming paralyzed fish. Unless indicated otherwise, all VR experiments used a constant forward-drifting grating to induce motor behavior. In closed loop, the visual scene was accelerated backward as fish attempted to swim; swim commands were detected from motor neuron axons with tail-attached electrodes. In open loop, the visual scene did not respond to swim commands. Dashed line, stationary grating; above dashed line, backward motion; Below, forward motion.

(C) Futility-induced passivity. In closed loop, fish swam naturalistically, at about one bout per second. In open loop, fish first swam with higher vigor, then stopped swimming for several to tens of seconds.

(legend continued on next page)

render swim efforts ineffective. The animals responded by first increasing their motor vigor, then suddenly stopping swimming, followed by cycling between passive and vigorously active behavioral states. To mediate such behavior, the brain must detect movement failures (when a motor command does not lead to perceived motion), integrate the failure signal over multiple attempts (to infer that the attempts are futile), and switch to another behavioral strategy. Using whole-brain imaging and targeted perturbations, we found that the noradrenergic (NE) system represents sensory-motor mismatch during movement failures, that radial astrocytes accumulate these NE mismatch signals, and that resulting surges in astrocytic activity activate downstream neurons and trigger behavioral passivity. These results show that radial astrocytes are fundamental to the rapid regulation of behavioral states.

RESULTS

Withholding Visual Feedback during Swimming Induces Passivity

Since swimming is central to fish behavior, we focused on the animal's response when it perceives that swimming is futile. We created this perception by withholding the visual feedback that normally accompanies motor output in a fictive swimming VR environment. After repeatedly attempting to swim with no change in visual flow, animals became passive (Figure 1A).

Animals (5–7 days post fertilization) were placed in a virtual environment where they fictively swam in response to forward-drifting visual scenes, as if against a water current, during which they attempted to stay in the approximate same spatial location (Orger et al., 2000; Rock and Smith, 1986; Vladimirov et al., 2014). In this "closed-loop" environment (Figure 1B), swim commands, measured from motor neuron firing in the tail, triggered backward visual flow like that seen during swim bouts. This elicited naturalistic swimming at a regular rate of about one swim bout per second (Dunn et al., 2016; Kawashima et al., 2016). The fish closely followed the visual stimulus, adjusting their swim vigor to compensate for changes in motosensory gain (i.e., coupling efficiency between swimming and visual feedback) (Ahrens et al., 2012; Portugues and Engert, 2011).

Fish were then switched to an "open-loop" protocol where forward visual flow was seen but swimming did not elicit visual feedback (Figures 1A and 1B). The animals increased swim vigor for many swim bouts but then abruptly became passive for a long time (Figures 1C and 1D), after which they resumed swimming, cycling between passive and active behavioral states lasting several to tens of seconds (Figure 1E). The animals also switched to a passive state when viewing replayed visual motion patterns in open loop that had been previously recorded during closed loop (Figure 1F), indicating that the passivity resulted from decoupling sensory feedback and behavior. Passive states (epochs when the animal did not swim for at least 5 s; Figures S1A and S1B) lasted 24.4 ± 2.5 s (mean ± SEM), and active states lasted 36.1 ± 4.2 s (n = 74; Figure 1H).

Several seconds prior to passivity, fish swam more vigorously and less frequently and attempted to make larger amplitude turns (Figures 1I and S1C). They were also passive when there was some, but very little, visual feedback (very low motosensory gain; Figure 1J).

Passivity was not due to fatigue, as similar swim vigor was accompanied by different passivity durations in the lowest gain range (Figures S1E and S1F). Nor was passivity due to struggles, as most passive periods were not preceded by struggling (Figures S1G–S1I). Thus, the crucial driver of the switch to passive behavior is the absence of visual feedback during swimming.

During passivity, fish were almost non-responsive to moving visual stimuli (Figures 1K and S1J), yet neuronal activity increased in the abducens nucleus, which controls eye movements (Figure S1K), suggesting that fish attempted to move their eyes more during this time.

The alternation of two opposing behavioral states allowed us to study the mechanisms of brain-state transitions.

Correlates of Passivity in Neuronal and Astrocytic Activity

We hypothesized that the passive state might be triggered by increased activity in cells that suppress swimming. We performed whole-brain cell-resolution calcium imaging in neurons and radial astrocytes during futility-induced passivity (Figure 2A). We used a light-sheet microscope (Ahrens et al., 2013; Panier et al., 2013; Vladimirov et al., 2014) with the VR environment to image animals expressing either GCaMP6f (Chen et al., 2013) or jRGECO1b (Dana et al., 2016) in almost all neurons under the *elavl3* promoter (Park et al., 2000) or in radial astrocytes under the *gfap* promoter (Bernardos and Raymond, 2006). We imaged either cell type or both with simultaneous dual-color imaging (STAR Methods).

When animals switched from the active to the passive behavioral state, whole-brain average neuronal activity decreased,

(D) Multiple trials of futility-induced passivity from a typical fish, showing passivity and switches to active behavior. Trials are successive epochs from a continuous recording, aligned by the onset of open loop.

(E) In prolonged open loop (tens of minutes), fish cycled between active and passive behavioral states.

(F) Futility-induced passivity also occurred when the stimulus seen in closed loop was replayed in open loop, showing that passivity was not caused by a change in the pattern of the visual motion. Dashed vertical lines indicate alignment of motor and sensory events on left and misalignment on right.

(G) Diagram with terminology for behavioral transitions.

(H) Mean duration (time between behavioral transitions) of active and passive epochs in prolonged open loop, n = 74 fish. An epoch is passive if the fish did not swim for 5 s or more (see Figures S1A and S1B). Error bars, SEM in all figures.

(I) Before the switch to passivity, inter-swim interval progressively increased, n = 61 fish (see Figure S1E).

(J) Prevalence of the passive behavioral state depended on the motosensory gain (coupling efficiency between swimming and visual feedback). Naturalistic gain (≈ 1) induced an active state. As the gain approached 0 (i.e., open loop), fish gradually spent more and more time in the passive state. n = 6 fish.

(K) Passive fish were less responsive to visual stimuli. Active or passive states were elicited via closed loop or open loop. Then a brief static stimulus was followed by brief forward motion. In passive fish, response to motion was reduced. Left: example. Right: population data. Two-tailed paired t test, $p = 4.2 \times 10^{-7}$, n = 11 fish (see Figure S1J).

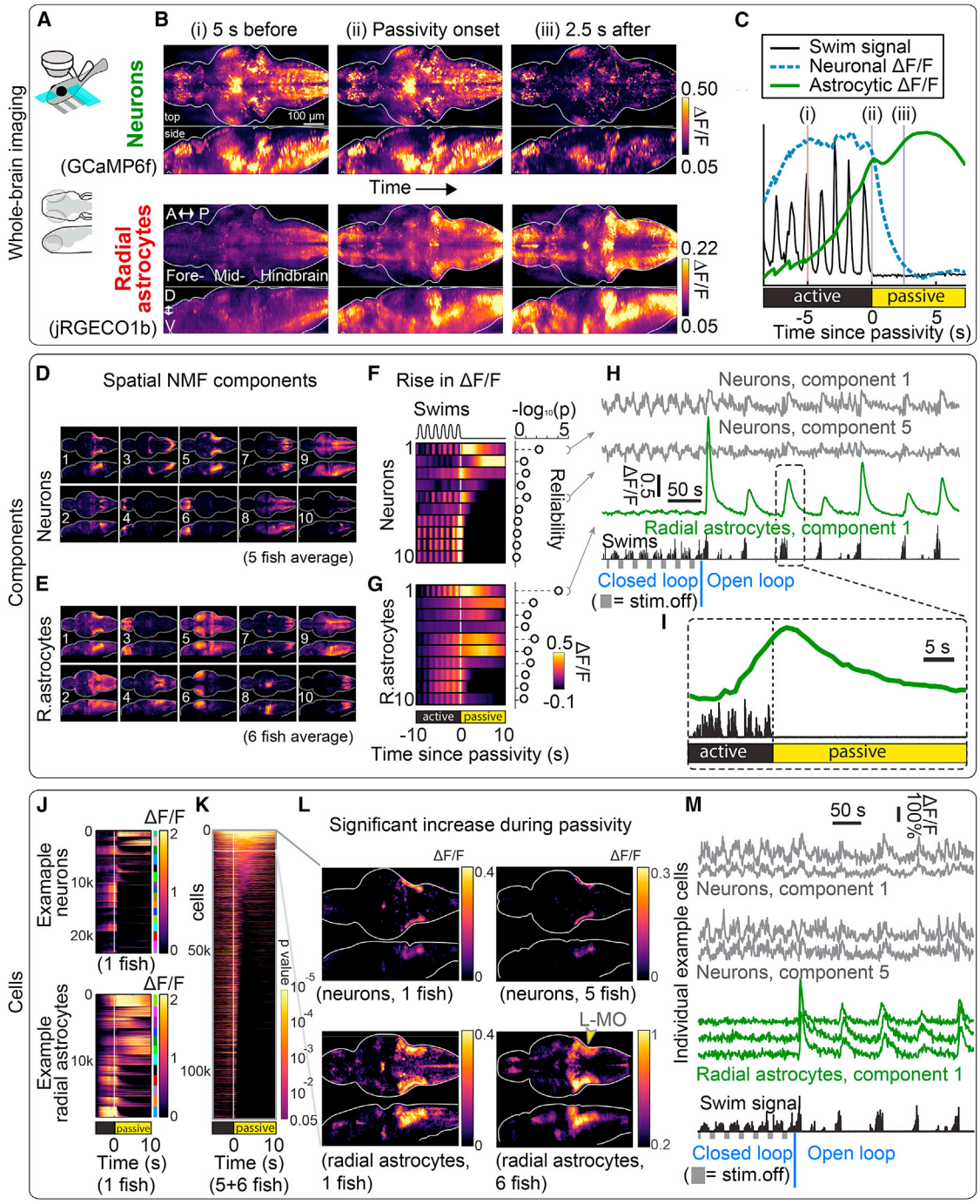

Figure 2. Whole-Brain Neuronal and Astrocyte Dynamics Show Ca^{2+} Increases in Specific Cell Populations during Futility-Induced Passivity

Figure360▷ For a Figure360 author presentation of this figure, see https://doi.org/10.1016/j.cell.2019.05.050.

(A) Experimental setup. A light-sheet microscope recorded from most radial astrocytes and neurons in the brain at cellular resolution, using either single-population GCaMP6f or simultaneous dual-color GCaMP6f and jRGECO1b recordings, while fictive behavior was monitored and visual stimulus was delivered.

(B) Whole-brain neuronal and glial activity before, at, and after passivity onset in an example *Tg(gfap:jRGECO1b); Tg(elavl3:GCaMP6f)* fish. Top: mean neuronal brain-wide activity was higher during active behavior than passivity. Bottom: conversely, mean brain-wide glial Ca^{2+} signals increased before passivity onset and remained elevated during passivity. A, anterior; P, posterior; D, dorsal; V, ventral. Images are maximum-intensity projections of means triggered on passivity onset (64 events).

(C) Neuronal and glial signals near passivity onset, averaged across the brain of the same fish from (B). Average neuronal Ca^{2+} decayed after passivity onset, while average glial Ca^{2+} increased before passivity onset and peaked soon after.

(legend continued on next page)

while glial activity increased (Figure 2B; Video S1). This increase in glial Ca^{2+} started seconds before passivity onset (Figures 2B and 2C). Both neuronal and glial Ca^{2+}, averaged across the brain, were higher and fluctuated more strongly in open loop than in closed loop (Figure S2A). Fluctuations in glial Ca^{2+} appeared strongest and most widespread during the first several switches to passivity in the minutes following the start of open loop, then became weaker and more localized.

To quantify these activity patterns in more detail and identify cell populations with similar activity patterns, we used non-negative matrix factorization (NMF) in neurons and radial astrocytes separately. A first round of NMF extracted single neurons, radial astrocytes, and segments of processes based on co-fluctuating activity of neighboring voxels (called "cell segments," or "cells" for brevity; STAR Methods). A second round factorized the brain into spatial components—sets of cells with coordinated activity (Figures 2D and 2E; Video S2)—and temporal components that describe the activity patterns of these cell groups (Figures 2F and 2G). We clustered the components into a set that occurred consistently across all fish (STAR Methods). Multiple components showed activity increases near the onset of passivity, including neuronal and glial components with elevated activity in the passive period (Figures 2F and 2G). A response reliability measure ($-\log_{10}$ p; STAR Methods) that quantifies consistency over repeated behavioral switches identified a consistent subset of glial signals (Figure 2G, component 1). Calcium in astrocyte component 1 increased before and peaked after passivity onset (Figures 2G–2I). When fish in a closed-loop protocol stopped swimming because the stimulus stopped moving, glial Ca^{2+} signals were weaker than during futility-induced passivity (Figure 2H). The most consistent surge in glial Ca^{2+} occurred in a neuropil-rich area in the lateral hindbrain, which we call area L-MO (lateral medulla oblongata, spanning rhombomeres 2–6, the area of astrocyte component 1 in Figure 2E; also called "neuropil area 4" in the Z-Brain atlas [Randlett et al., 2015] and regions #12 and #171 in Zebrafish Brain Browser [Marquart et al., 2015]).

Finally, we analyzed single-cell segments. Ca^{2+} signals from neurons and glia were analyzed near passivity onset (Figure 2J). For each cell, we used a p value to quantify the consistency of Ca^{2+} increases above baseline (Figure 2K; Video S3; STAR Methods). Of all brain regions, L-MO radial astrocytes showed the most consistent increases in activity during passivity (Figure 2L) and showed ramping Ca^{2+} signals before passivity onset (Figures 2G, 2I, 2M, and S2C–S2E). Similar glial Ca^{2+} activity occurred in another futility-induced passivity assay, where untethered fish become passive after being submerged in a viscous agarose solution (Figure S2F; Video S4).

Astrocytic Ca^{2+} started to increase before the switch to passivity (Figures 2G, 2I, and S2C–S2E). This Ca^{2+} elevation and the peak that followed at passivity onset led us to hypothesize that radial astrocytes may suppress swimming.

Anatomy of Radial Astrocytes

To provide anatomical context for these observations, we examined the morphology of radial astrocytes extending processes to the L-MO. In fish expressing GCaMP6f in radial astrocytes, some residual GCaMP6f may remain in newly differentiated neurons (Anthony et al., 2004; Fujita et al., 2014; Sloan and Barres, 2014). We examined protein expression driven by *gfap* and *elavl3* promoters and found them well segregated across the brain (Figures S3A and S3B), suggesting, together with the differences in Ca^{2+} activity (Figures 2F and 2G), that neuronal and glial Ca^{2+} measurements were well separated.

In *gfap* transgenics (Figures 3A–3C), we filled single radial astrocytes with dye to visualize their morphology (Figure 3D). The cell bodies resided in the dorsal midline of the hindbrain in rhombomeres 2–6, and the bushy processes resided in L-MO; the Ca^{2+} signals locked to passivity originate in these processes (Figures 3 and S3C–S3F). These processes ramify throughout the L-MO neuropil and appose GABAergic cell bodies at the edge of the brain (Figure 3D). The GCaMP6f signal in the L-MO can spread to the cell bodies (Figure 2D, radial astrocyte components 1→2→4; Video S1) through the connecting processes. Activation of other brain areas (e.g., glial components 3, 5, 6) happened more often right after transitions from a closed-loop to an open-loop protocol. Radial astrocytes lacked active membrane properties and had a more negative resting-membrane potential than neurons (Figure S3G), consistent with previous observations of these cells (Li et al., 2015).

(D and E) Spatial NMF components. Neuronal and glial data recorded with GCaMP6f in separate transgenic lines. Brightness: spatial NMF weights. n = 5 fish (neurons), n = 6 fish (radial astrocytes).

(F and G) Temporal neuronal and glial Ca^{2+} signals, per NMF component of (D) and (E), averaged over fish and trials, centered on passivity onset. Right: reliability ($-\log_{10}(p)$), calculated by comparing Ca^{2+} activity 1–4 s after passivity onset to mean activity 10–5 s before passivity onset (higher reliability: more consistent responses over trials). Multiple neuronal and glial components had strong correlations to behavior. Neuronal and glial component 1 overlaps with L-MO.

(H) Signals from example fish; see also Figure S2B. Fish was first in closed loop, presented with alternating moving and stationary gratings (fish swam little during stationary gratings), and next in open loop, wherein animals cycled through active and passive states. Radial astrocytes were engaged in switches to passivity in open loop, not swim pauses in closed loop.

(I) Astrocytic signal from (H), showing a rise before and peak after passivity onset.

(J) Cellular signals from segmented neurons and glia from two example fish, grouped by component (colored bars, right), relative to passivity onset.

(K) Neurons and glia (random subset) from all fish with elevated signals after passivity onset, ordered by p value from a statistical test of how reliably Ca^{2+} is increased above baseline (10–5 s before passivity).

(L) Brain maps of neurons and radial astrocytes with reliably elevated Ca^{2+} just after passivity onset (1–4 s) relative to baseline. L-MO signals were most consistently above baseline across fish. Left: example. Right: population average (5 fish for neurons, 6 for glia, registered to standard brain). p values were not used to test statistical significance but to create an exploratory functional brain map (STAR Methods).

(M) Ca^{2+} traces from single cells, same fish as in (H) and (I), during closed loop (left) and open loop (right). Radial astrocytes selectively respond to futility-induced passivity.

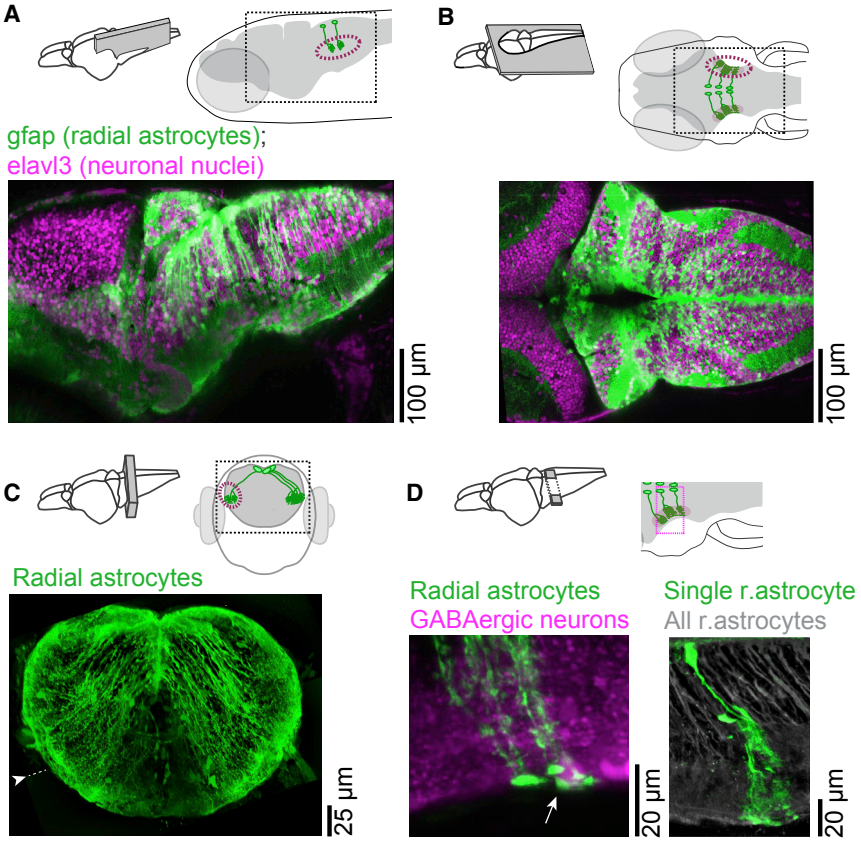

Figure 3. Morphology of Radial Astrocytes Projecting to L-MO

(A) Maximum intensity projection (MIP) along the medial-lateral axis of a 20 μm section from *Tg(elavl3:H2B-GCaMP6f);Tg(gfap:tdTomato)* fish. Dashed line, L-MO location. Neurons, magenta; glia, green.

(B) MIP along dorsal-ventral axis of a 20 μm section, same fish as (A). Radial astrocytes ramify in L-MO.

(C) MIP along the rostral-caudal axis of a 20 μm section in hindbrain. Radial astrocyte processes project ventral-laterally. Scale bar is corrected for 4× expansion (Freifeld et al., 2017; Tillberg et al., 2016) to approximate *in vivo* dimensions. Arrowhead indicates microscopy software stitching artifact.

(D) MIP along dorsal-ventral axis. Diagonal section with one (right) or several (left) radial astrocytes electroporated with synthetic dye. Astrocytic somata are proximal to dorsal midline of hindbrain; their processes run ventral-laterally, are dense in lateral hindbrain (green at brain border), and appose GABAergic somata (left: white arrow, magenta, labeled by *Tg(gad1b:RFP)*); radial astrocytes (right: gray) labeled by *Tg(gfap:jRGECO1b)*.

Radial Astrocyte Activation Increases Passivity; Silencing Decreases Passivity

Since radial astrocytes were activated before and at the transition from active to passive states, we asked whether disabling these cells prevents the behavioral-state transition and whether activating them triggers it. We used two-photon laser ablation to kill glial cells projecting to L-MO (Vladimirov et al., 2018) (~300 of ~1,000 such cells, using nuclear-localized GCaMP6f under the *gfap* promoter to target somata; STAR Methods) (Figure 4A) and assayed for futility-induced passivity. Ablated animals spent half as much time in the passive state as they did before ablation (Figures 4B and 4C), suggesting that radial astrocytes are necessary to trigger passivity. We confirmed that this effect was not restricted to fictive swimming: when deprived of visual feedback during tail motion, nonparalyzed head-embedded fish were more active after ablation (Figures 4D and S4A–S4C). This behavioral change was specific to radial astrocyte ablation, since ablation of either a matched number of neurons in random locations or a large part of the forebrain (STAR Methods) did not affect futility-induced passivity (Figures 4E, S4D, and S4E). This effect was not due to hyperactivity, since fish with glial ablation can still stop swimming and perform motor adaptation (Figures S4F and S4G). An additional nitroreductase-based chemogenetic approach to render radial astrocytes unhealthy (Tabor et al., 2014) also reduced passivity (Figure S4H). Thus, futility-induced passivity depends on the presence of healthy, functioning radial astrocytes.

Since astrocytes support neuron health (Banker, 1980; Lyons and Talbot, 2014), we controlled for adverse effects of glial ablation on neurons. After ablations, we observed no significant difference in swim frequency, power, or velocity in freely swimming fish (Figure 4F). Also, neural activity in L-MO was similar before and after glial ablation during closed-loop fictive swimming (Figure 4G), suggesting that the targeted ablation minimally affects neural activity outside of futility-induced passivity.

Finally, we blocked the inositol 1,4,5-trisphosphate receptor (IP_3R) to reduce Ca^{2+} release from intracellular stores in radial astrocytes. Ca^{2+} transients dropped (Figure S4I) when we locally puffed the IP_3R inhibitor xestospongin C (XeC) onto astrocytic cell bodies in the dorsal midline of the hindbrain (Figure 4H). We minimized exposure of neurons to XeC by injecting into a region containing mostly glia. This inactivation method also reduced futility-induced passivity (Figure 4H).

Together, these results strongly suggest that radial astrocytes are necessary for futility-induced passivity.

To test whether surges in astrocytic Ca^{2+} are sufficient to reduce swimming, we used a chemogenetic approach to increase intracellular Ca^{2+} in glia. We transiently expressed rat TRPV1 in a sparse subset (~1%) of radial astrocytes (Figure S5A; STAR Methods), rendering their membranes highly permeable to Ca^{2+} upon exposure to the agonist, capsaicin (other cells were unaffected since, unlike rat TRPV1, the zebrafish ortholog is insensitive to capsaicin) (Chen et al., 2016; Munns et al., 2015). We targeted only a tiny subset of cells to mitigate any unphysiological effects of TRPV1 activation. Application of capsaicin (5 μM) caused increased Ca^{2+} fluctuations in the population (Video S5), potentially through gap junctions (Fujii et al., 2017). The fish became passive more than 60% of the time, starting

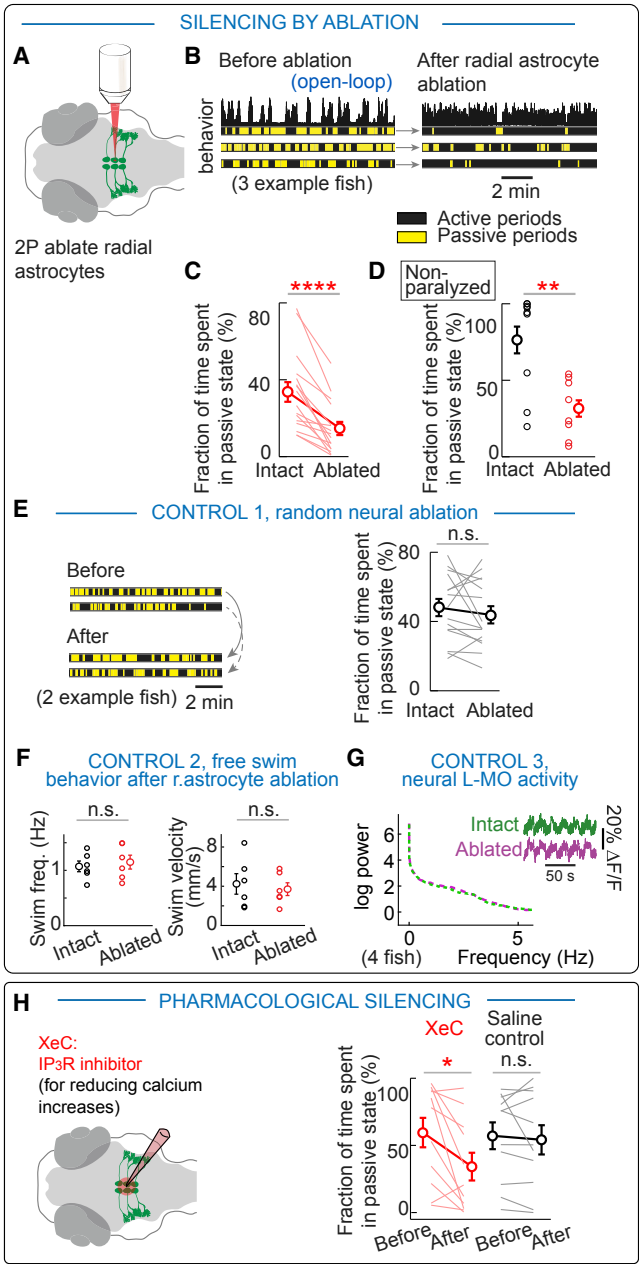

Figure 4. Radial Astrocytes Are Necessary for Futility-Induced Passivity

(A) Experimental design. ~300 astrocytes projecting to L-MO were ablated with a 2-photon laser with single-cell resolution, in fish with radial astrocytic nuclei fluorescently labeled. In all following panels, n.s., not significant; *p < 0.05; **p < 0.01; ***p < 0.001; ****p < 0.0001.

(B) Reduced futility-induced passivity after glial ablation in 3 example fish.

(C) Population data showing a ~50% reduction in futility-induced passivity. Two-tailed paired t test, $p = 1.3 \times 10^{-5}$, n = 16.

(D) Alternative assay for futility-induced passivity: unparalyzed, head-restrained tail-free also show passivity. Fish with ablated astrocytes remained active most of the time (Figures S4A–S4C). Two-tailed non-paired t test, p = 0.0041, n = 8 fish in both conditions.

(E) Ablation of ~300 random neurons had no significant effect on passivity. Two-tailed paired t test, p = 0.34, n = 15 fish.

(F) Control for nonspecific effects of astrocytic ablation. During free swimming, ablated fish showed no abnormalities in swim frequency or velocity. Two-tailed non-paired t test, p = 0.75 for swim frequency, p = 0.67 for swim velocity, n = 6 fish.

(G) Imaging in L-MO before and after glia ablation showed no difference in neural activity in closed loop with alternating moving and stationary gratings. Inset, example activity; main panel, power spectral density. n = 4 fish.

(H) Reducing glial Ca^{2+} by blocking IP_3R reduced futility-induced passivity. XeC (100 μM inside pipette) or saline was puffed onto astrocytic somata. Two-tailed paired t test, p = 0.033, p = 0.54, n = 11 fish in both conditions.

when surges in astrocytic Ca^{2+} appeared (Figures 5A–5D) in a closed-loop environment with drifting gratings (where the normal passive time is 2.3% ± 1.2%). L-MO glial Ca^{2+} rose before passivity and peaked shortly thereafter (Figure 5E). This effect was absent when capsaicin was applied to fish without TRPV1 or saline to fish with TRPV1 (Figures 5F–5H). The temporal dynamics of capsaicin-triggered glial Ca^{2+} increases at passivity onset resembled those triggered by open loop in TRPV1-negative fish (Figure 5I), suggesting that TRPV1 evokes a naturalistic process. Unlike the switch to passivity induced by open loop, capsaicin-induced switching was not preceded by increased swim vigor (Figure S5B). Thus, surges in Ca^{2+} in L-MO radial astrocytes alone appear sufficient to stop swimming.

To test with temporal precision whether activating radial astrocytes suppresses swimming, we expressed CoChR (Klapoetke et al., 2014), a large-current channelrhodopsin, in radial astrocytes and activated it by shining blue light on L-MO with a digital micromirror device (DMD) (Zhu et al., 2012a). The resulting increase in glial Ca^{2+} (Figures 5J and S5C; Video S5) looked natural, including in its wave-like propagation (Figure S5C). However, opening this channel might elicit concomitant changes in intracellular sodium levels and pH, and although we did not detect double-labeled cells, neurons may express residual low levels of CoChR (Anthony et al., 2004; Fujita et al., 2014; Sloan and Barres, 2014). Hence, in another experiment, we expressed the optogenetic G protein-coupled receptor (GPCR) Opto-α1-AR (Airan et al., 2009) in radial astrocytes to mimic the Gq-coupled human α_{1a}-adrenergic receptor; in this case, exposure to blue light increased glial Ca^{2+}. Even if there were residual expression in neurons, this manipulation was unlikely to drive spikes due to relatively low efficiency and the indirect relationship between GPCR signaling and spiking. Both CoChR and Opto-α1-AR (Figure 5J) activation (Figueiredo et al., 2014) induced a drop in swim power (beyond a first mild drop also in controls, perhaps as the fish sees scattered blue light) (Figures 5K–5P, S5D, and S5E).

Thus we showed, with six different gain- and loss-of-function experiments, that activation of radial astrocytes can suppress swimming (Figure 5Q; caveats and controls in Table S1) and trigger the passive behavioral state.

Radial Astrocytes Drive Activity in GABAergic Neurons that Inhibit Swimming

We reasoned that any effect of an elevation in astrocytic Ca^{2+} on behavior must occur via neurons. Neurons at the edge of L-MO are reliably activated at passivity onset (Figures 2D, neuronal component 1, and S5F), suggesting that their activity increase is due to astrocytic Ca^{2+} increases. Supporting this

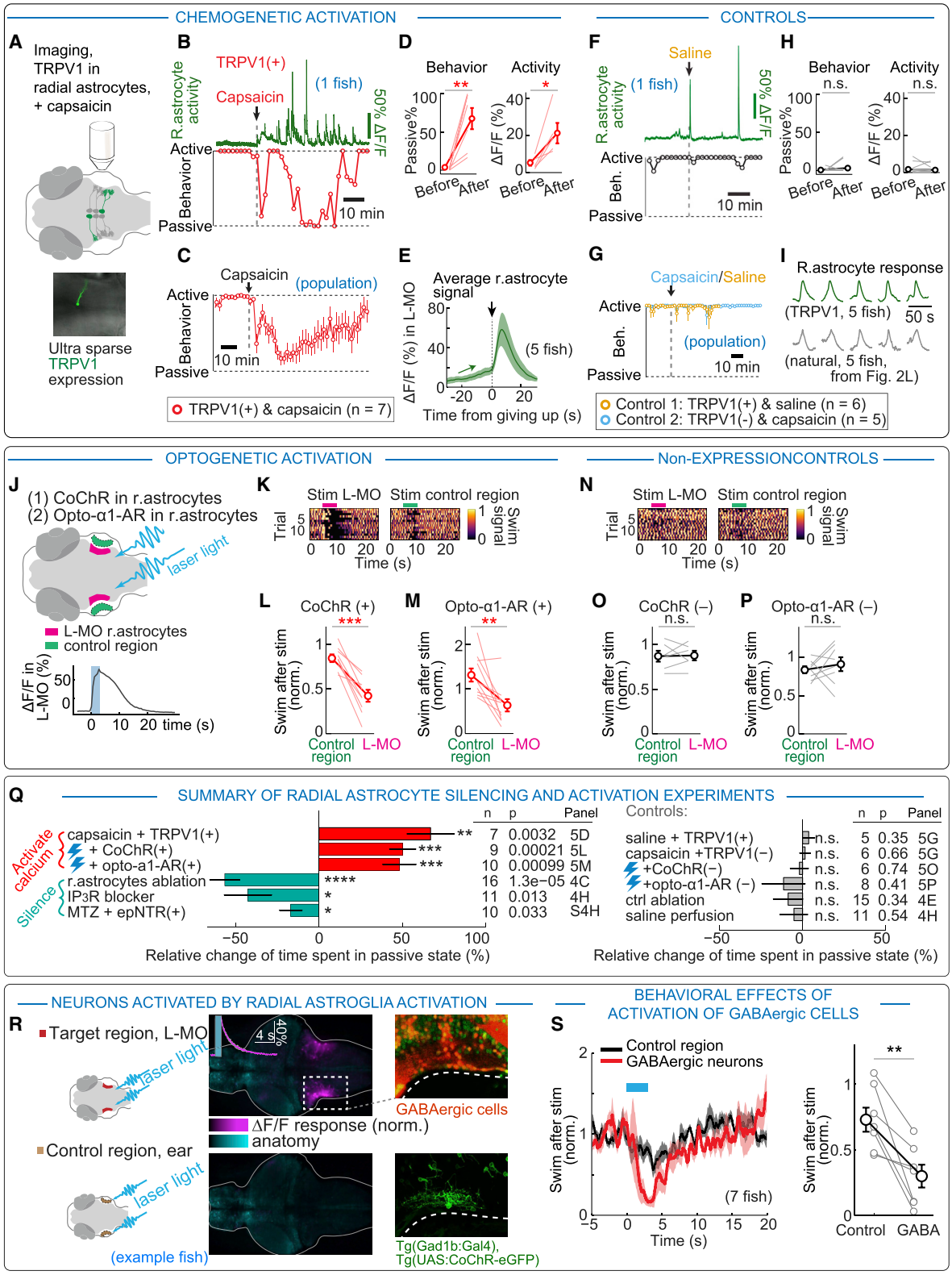

(legend on next page)

idea, increasing astrocytic Ca^{2+} by either CoChR or TRPV1 activates neurons at the edge of L-MO (Figures 5R, S5G, and S5H). Optogenetic activation of these neurons, which are GABAergic with processes innervating L-MO (Figure 5R), also suppressed swimming (Figure 5S). These results provide evidence that L-MO radial astrocytes activate GABAergic neurons at the edge of L-MO and suggest that these cells in turn suppress swimming.

The Noradrenergic System Conveys Swim Failures to Radial Astrocytes

Futility-induced passivity results from multiple motor failures, which must be communicated to radial astrocytes by neurons. We hypothesized that the NE system might drive radial astrocytic Ca^{2+} signals based on known relationships of norepinephrine to behavior (Sara, 2009) and its effect on astrocytes (Bekar et al., 2008; Ding et al., 2013; Ma et al., 2016; Paukert et al., 2014; Slezak et al., 2018). We found that neurons in the locus coeruleus (LC) and the NE cluster of the medulla oblongata (NE-MO; Figures 6A and S6A) (Farrar et al., 2018; Tay et al., 2011) increased activity before switches to passivity. We imaged Ca^{2+} in NE neurons and in glia simultaneously in *Tg(th-P2A-Gal4); Tg(UAS:GCaMP6s); Tg(gfap:jRGECO1b)* fish. During futility-induced passivity, signals from NE neurons and glia were temporally coupled, with NE cell responses preceding astrocytic responses (Figures 6B and 6C; Video S6).

Radial astrocytes express multiple NE receptors (Table S2; Figure S6B), and NE axons project to L-MO (Figure S6C; Video S6), indicating that glial processes in L-MO could be driven by NE neurons.

Ablating NE-MO with a two-photon laser greatly reduced time spent in passivity, but no significant reduction resulted from ablation of the LC; ablation of the serotonergic dorsal raphe nucleus (DRN) also did not result in a significant change (Figures 6D–6F). Thus, the NE-MO, which may be homologous to NE cluster A2 in mammals (Rinaman, 2011), is necessary for futility-induced passivity.

To directly test whether NE-MO activates radial astrocytes and triggers passivity, we optogenetically activated NE-MO while imaging radial astrocytes (Figure 6G) (Zhu et al., 2012a) in fish expressing CoChR in NE cells and jRGECO1b in radial astrocytes (*Tg(dbh:KalTA4); Tg(UAS:CoChR-eGFP); Tg(gfap:jRGECO1b)*). This led to Ca^{2+} responses in glial processes in L-MO and induced passivity for ~10 s (Figures 6H and 6I). In fish with radial astrocytes ablated (as in Figures 4A–4C), activation did not lead to passivity (Figures 6I and S6E), showing that passivity resulting from artificial NE-MO activation also requires radial astrocytes.

We then identified the NE receptor that activates radial astrocytes (RNA sequencing, Table S2). After adding prazosin (α1-adrenergic receptor antagonist, 50 μM) or cyclazosin (α1B receptor antagonist, 10 μM), optogenetic activation of NE-MO no longer caused radial astrocyte activation (Figures 6J–6L). Puffing an α1 agonist elicited Ca^{2+} responses, and blocking the α2 receptor did not eliminate Ca^{2+} signals (Figures S6F and S6G). Thus, the response of L-MO radial astrocytes to NE is mediated by the α1B adrenergic receptor.

Finally, we tested whether astrocytic Ca^{2+} responses were driven solely by NE or by a combination of NE and local circuit activity like mammalian astrocytes in visual cortex (Paukert et al., 2014). We used swimming, which correlates with L-MO neural activity, as a proxy for local circuit activity (Figure 6M). Activating NE-MO during swimming caused a greater glial response than activating NE-MO without swimming (Figure 6N). Thus, radial astrocyte Ca^{2+} integrates NE and local circuit activity.

Figure 5. Activation of Radial Astrocytes Reduces Swimming

(A) Experimental design. Rat TRPV1 was expressed in ~1% of radial astrocytes in *Tg(gfap:jRGECO1b)* fish. Fish were exposed to the TRPV1 agonist capsaicin.

(B) Example fish with increased Ca^{2+} transients in L-MO and concurrent increase in passivity after capsaicin treatment. The effect diminished after ~1 h, maybe due to TRPV1 desensitization and internalization (Sanz-Salvador et al., 2012), showing that fish remain healthy, as they can swim normally. Dashed line (passive) means the fish is passive 100% of the time; dashed line (active) means it is passive 0% of the time (both measured in 2 min bins).

(C) Population data, showing increased passivity after activation of TRPV1. n = 7 fish.

(D) Population data of L-MO astrocytic Ca^{2+} increase and passivity with TRPV1 activation. Two-tailed paired t test, behavior: p = 0.0029, n = 7 fish. $\Delta F/F$: p = 0.027, n = 5 fish.

(E) Astrocytic Ca^{2+} in L-MO near passivity onset. Average signal increased just before passivity onset and peaked just after, as in futility-induced passivity (Figures 2G–2I). Shading, SEM.

(F) Control, example. No reduction of swimming or increase in astrocytic Ca^{2+} when saline was added to fish expressing TRPV1.

(G) Control, population data. No change in behavior when saline was added to fish expressing TRPV1 (n = 6 fish) or capsaicin to fish without TRPV1 (n = 5 fish).

(H) Summary of controls. Experiments as in (F) and (G) were pooled. Two-tailed paired t test, behavior: p = 0.48, n = 11 fish. $\Delta F/F$: p = 0.51, n = 7 fish.

(I) Normalized mean L-MO glial Ca^{2+} signals centered on the onset of passivity, induced by TRPV1 in closed loop (top) or by motor futility in open loop (bottom). Surges appear similar. Ca^{2+} in TRPV1+ animals did not saturate.

(J) Experimental design. Local optogenetic excitation of glial processes in fish expressing CoChR or Opto-α1-AR increases glial Ca^{2+} in L-MO (CoChR shown).

(K) Optogenetic (CoChR) excitation of L-MO glia reduced swimming for ~10 s. Blue light outside the brain caused a much milder and briefer reduction.

(L and M) Population data show reduced swimming relative to controls in fish expressing CoChR (L) or Opto-α1-AR (M) in radial astrocytes. Two-tailed paired t test, CoChR, p = 0.00012, n = 9 fish; Opto-α1-AR, p = 0.0065, n = 10 fish.

(N–P) Controls for (K)–(M) show no effect in fish without CoChR or Opto-α1-AR. Two-tailed paired t test, CoChR: p = 0.89, n = 6 fish. Opto-α1-AR, p = 0.50, n = 8 fish.

(Q) Summary of Figures 4 and 5, showing significant increases in passivity after increases in astrocytic Ca^{2+}, decreases after astrocytic silencing, and no effects in control experiments. Effects are normalized by maximal possible change (control passive % for decreases; control active % for increases) for each fish.

(R) Optogenetic activation of L-MO radial astrocytes activates GABAergic neurons at edge of L-MO in *Tg(gfap:CoChR-eGFP);Tg(elavl3:jRGECO1b)* fish. Left: maximum-intensity projection of $\Delta F/F$ after optogenetic activation of radial astrocytes (magenta) and anatomy (cyan) in example fish. Inset: Ca^{2+} in GABAergic neurons after astrocytic activation; stimulation time in cyan. Top right: *Tg(gad1b:RFP);Tg(elavl3:H2B-GCaMP6f)* used to label GABAergic neurons; bottom right: *Tg(gad1b:Gal4);Tg(UAS:CoChR-eGFP)* to sparsely label GABAergic neurons.

(S) Activation of GABAergic cells with laser light in *Tg(Gad1b:Gal4);Tg(UAS:CoChR-eGFP)* suppresses swimming. Two-tailed paired t test, p = 0.0074, n = 7 fish.

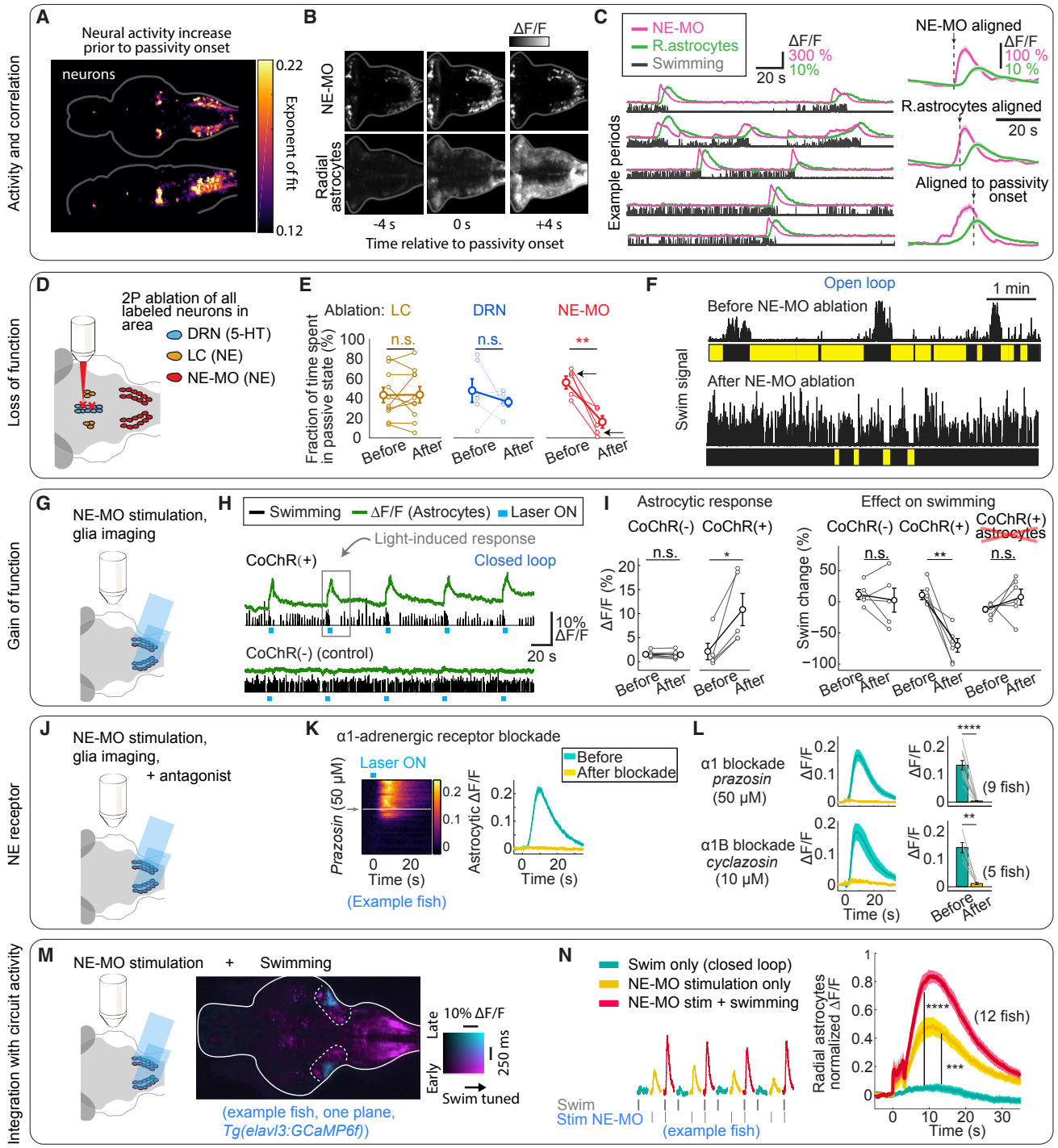

Figure 6. Noradrenergic System Activates Radial Astrocytes and Is Required for Futility-Induced Passivity

(A) Rate of neuronal activity increase before passivity onset quantified by the exponent of an exponential fit to average Ca^{2+} signals before passivity (overlay of 5 fish, *Tg(elavl3:GCaMP6f)*). Population with the highest rate of increase overlaps with NE neurons (see Figure S6A).

(B) Simultaneous imaging of NE neurons and radial astrocytes. Example Ca^{2+} signals just before, at, and after passivity onset.

(C) Examples of NE-MO activity, glial Ca^{2+} increases, and swimming in an alternating closed- and open-loop protocol. Right: average Ca^{2+} activity from NE-MO and radial astrocytes, aligned to NE-MO response onset, radial astrocyte response, or passivity onset.

(D) Experimental design: single-cell 2-photon ablation of LC, NE-MO, or DRN in transgenic zebrafish labeling these nuclei.

(E) Time in passivity was strongly reduced after NE-MO ablation, but not after ablation of LC or DRN. Two-tailed paired t test, p = 0.95, n = 10 fish for LC; p = 0.40, n = 6 fish for DRN; p = 0.0070, n = 5 fish for NE-MO.

(legend continued on next page)

What information does NE convey to radial astrocytes? If L-MO radial astrocytes encode swim futility (the time integral of failures), we hypothesized that the NE system encodes swim failures. To look for such signals, we imaged NE cells in three conditions, randomly interleaved over swim bouts: (1) fictive swimming in closed loop with backward visual flow to mimic "successful" swimming (92% of swims), (2) backward visual flow without swimming (4%), and (3) swimming in open loop without visual feedback (4%) to mimic "failed" swims (Figure 7A). If NE cells detect mismatch (Keller et al., 2012), they should be more activated in (3) than in (1) or (2). Indeed, that is what we found (Figure 7B): NE-MO responses were small or absent when fish swam with naturalistic feedback but large when they swam without feedback.

We next quantified whether NE-MO responses encode the difference between perceived and expected visual feedback during swimming. We randomized motosensory gain to elicit successful swims (gain > 0; swim generates backward visual motion) and failed swims (gain $\leq$ 0; swim with no visual change or motion opposite to expected; Figure 7C). NE-MO responses were consistent with a mismatch signal, increasing when motor vigor increased without visual effect (Figures 7D and 7E), or when vigor was constant and backward visual flow was absent or forward flow was seen (Figures 7F and 7G). Thus, NE-MO signals swim failures by encoding sensory-motor mismatch.

Radial Astrocytes Integrate Evidence that Actions Are Futile

Determining that a behavior is futile requires integrating the results of multiple successive attempts. Failed swims lead to elevated NE-MO activity, which in turn excites astrocytes (Figure 7H). NE-MO Ca^{2+} eventually leveled out or decreased (Figures 7H and 7I), while astrocytic Ca^{2+} continued to increase (Figures 7H and 7I). As radial astrocytes respond to sensory-motor mismatch signals from NE-MO and accumulate them over time, we asked whether they integrate evidence (Pinto et al., 2018; Shadlen and Newsome, 2001) that actions are futile. We designed a behavioral task in which swimming leads to visual flow probabilistically (Figure 7J). First, in closed loop, all swim bouts trigger visual flow. Next, every swim bout triggers visual flow with probability P. Glial Ca^{2+} rose fastest when P = 0 (always futile), did not rise when P = 1 (always effective), and increased at intermediate rates for intermediate P (Figure 7K). This shows that, following a switch from a closed-loop to a stochastic feedback protocol, radial astrocyte Ca^{2+} reflects evidence accumulation. Together, these results (Table S3) show mechanistically how radial astrocytes encode experience and control behavioral state.

DISCUSSION

Here, we found that the fish analog of the mammalian astrocyte is a central computational element of a circuit implementing a behavioral-state change after integrating sensory information. Specifically, radial astrocytes in a subregion of the brainstem in larval zebrafish temporally integrate noradrenergically encoded failures to accumulate evidence of futility before inducing a state of passivity ("giving up"). This behavioral pattern has a familiar combination of features: trying to achieve a goal, repeatedly failing despite trying harder, giving up temporarily, and then trying again—fish swim more vigorously in open loop (i.e., ineffective swim attempts), become passive, then swim again. Using whole-brain imaging, we found that astrocytic calcium was elevated just before—and during—passive states. Activation and silencing experiments established that these glial cells are required to trigger the passive state. Neuronal imaging and manipulation showed that the NE system encodes an expectation-outcome mismatch signal, which activates Ca^{2+} signaling in radial astrocytes. Thus, behavioral failures are detected by NE-MO and integrated by glia, which, after accumulating sufficient evidence of motor futility, trigger a passive behavioral state via GABAergic neurons. Once passivity is triggered, its persistence may be due to sustained effects of the glial cells on neurons, or a lag in the reactivation of swim circuits. These results imply that routinely including astrocytes in systems neuroscience studies may accelerate achieving a comprehensive understanding of brain function (Barres, 2008).

This study extends the known roles of glial cells to include a specific computation (temporal integration of a behaviorally relevant mismatch signal), resulting in a direct, fast effect on brain and behavioral state (induction of passivity within seconds). The traditional view of astrocytes as supporting cells for neurons is known to be incomplete (Araque et al., 2014; Kjaerby et al., 2017), as they actively influence neuronal activity.

(F) Example shows NE-MO ablation reduced futility-induced passivity. Arrows in (E), corresponding data points.

(G) Experimental design: optogenetic activation of NE-MO cells using DMD-targeted light delivery in fish expressing CoChR in NE cells while imaging radial astrocytes expressing jRGECO1b.

(H) Example fish, NE-MO activation led to increased L-MO glial Ca^{2+}, then passivity. Swimming increases briefly at light onset (see Figure S6D).

(I) Population data: NE-MO activation increased L-MO glial Ca^{2+} (left) and reduced swimming (right) in $CoChR^{+}$ fish. Two-tailed paired t test, $CoChR^{+}$ imaging, p = 0.025, n = 5 fish; $CoChR^{+}$ behavior, p = 0.0024, n = 6 fish; $CoChR^{-}$ imaging, p = 0.52, n = 7 fish; $CoChR^{-}$ behavior, p = 0.56, n = 5 fish; glial ablation, p = 0.27, n = 6 fish.

(J) Experiment to identify receptors. Experiment as in (G) with NE receptor antagonists added to bath.

(K) α1 NE receptor antagonist prazosin (50 μM) abolishes radial astrocyte response evoked by NE-MO stimulation.

(L) Population data. α1 NE receptor antagonist prazosin (50 μM) or α1B antagonist cyclazosin (10 μM) abolished radial astrocyte responses. Two-tailed paired t test, prazosin, $p = 4.6 \times 10^{-5}$, n = 9 fish; cyclazosin, p = 0.0042, n = 5 fish. Shading, SEM.

(M) Experimental design to test whether L-MO radial astrocytes integrate NE and local circuit activity. In closed loop, NE-MO cells are optogenetically stimulated during swimming (higher L-MO neuronal activity), or during not swimming.

(N) Integration of NE and local circuit activity. Radial astrocytic Ca^{2+} responses to NE during swimming are larger than to NE alone. Left: examples from successive trials. Right: summary of all fish. Two-tailed paired t test, $p = 2.4 \times 10^{-4}$ for NE-MO stimulation only versus swimming only, $p = 2.4 \times 10^{-8}$ for NE-MO stimulation + swimming versus swimming only, n = 12 fish. Shading, SEM.

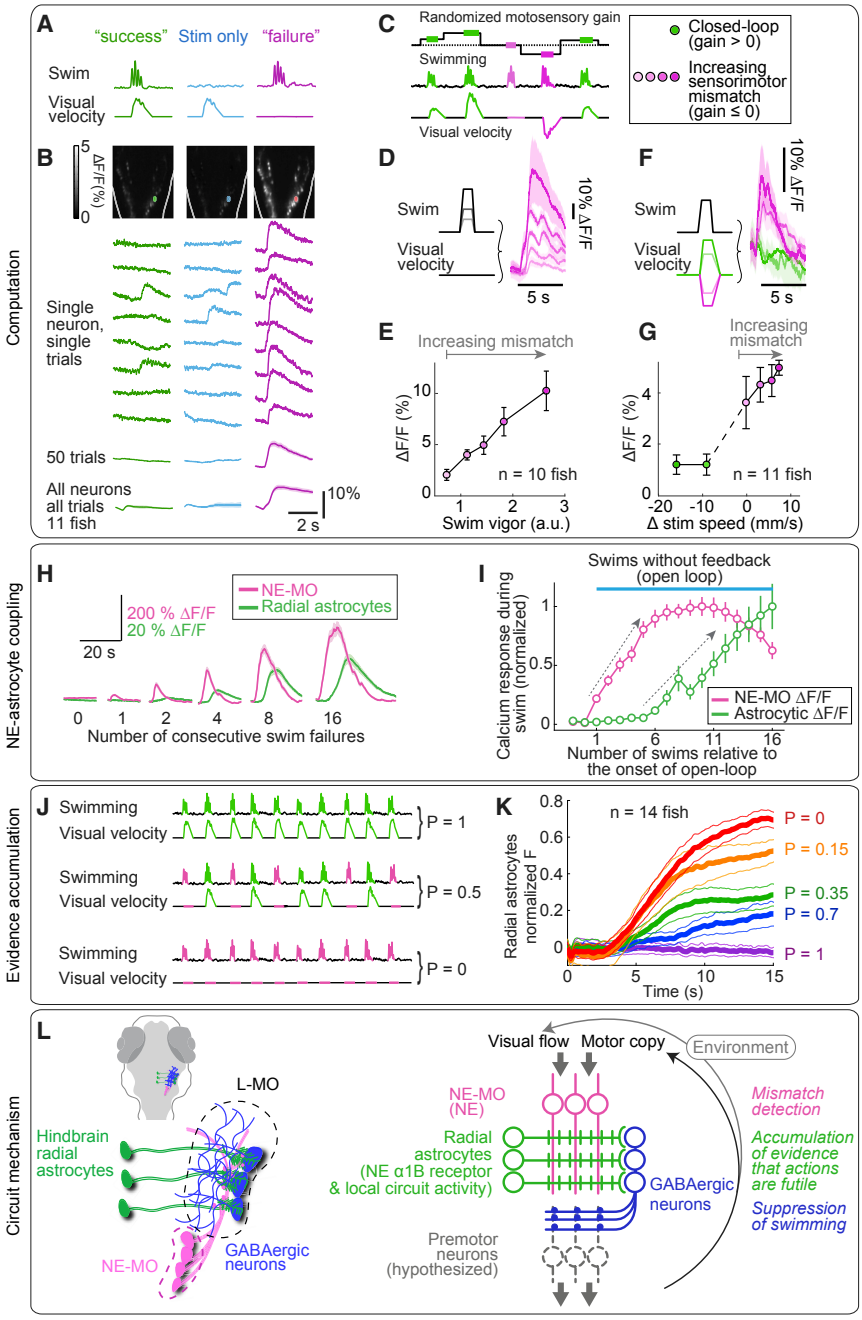

Figure 7. Noradrenergic System Signals Visuomotor Mismatch; Radial Astrocytes Accumulate Evidence that Actions Are Futile

For a Figure360 author presentation of this figure, see https://doi.org/10.1016/j.cell.2019.05.050. Figure360▷

(A) Mismatch assay. Left: in closed loop, motor output triggers visual feedback (motosensory gain > 0). Middle: stimulus only with no swimming. Right: sensory-motor mismatch in swim failures (gain = 0).

(B) Mismatch signals in NE-MO. In closed loop or visual signal alone, NE-MO responses were small. During swim failures, NE-MO responses were large. (See Figure S6H for LC, which does not respond to mismatch until next swim bout.)

(C) Extended mismatch assay: motosensory gain randomly set for each swim bout, varying combinations of motor vigor and visual velocity.

(D–G) NE-MO responses encode sensory-motor mismatch. (D and E) NE-MO responses grew with stronger motor vigor if no visual stimulus was shown. (D, example fish; E, population data, 10 fish.) (F and G) NE-MO responses were minimal in closed loop (motosensory gain > 0), whether gain was high or low. In open loop (no feedback, gain = 0) NE-MO responded. With opposite feedback (forward visual feedback during swimming, high mismatch, motosensory gain < 0), NE-MO response was larger. In (F and G), average motor vigor is similar across visual speeds due to randomization of gain. (F, example fish; G, population data, 11 fish). Shading, SEM.

(H) Radial astrocyte Ca^{2+} integrates swim failures. Fish swam in closed loop, then open loop for 1, 2, 4, 8, or 16 swim bouts, then back to closed loop. Glial signals increased with number of failed bouts after ~2 failed bouts; NE-MO signals began increasing with first failed bout. Trials with passivity not included. NE-MO signal sometimes saturated or decreased while glial Ca^{2+} continued to increase.

(I) Radial astrocyte Ca^{2+} accumulated with increasing numbers of swim failures. NE-MO Ca^{2+} also increased initially but saturated or decreased, while glial Ca^{2+} continued to increase with swim failures until feedback returns to closed loop. Gray arrows, accumulation.

(J) Experiment: information accumulation in radial astrocytes. In a swim bout, probability that fish sees visual feedback (backward visual flow) is P. P = 1, closed loop; P = 0, open loop; intermediate P gives probabilistic feedback.

(K) Information accumulation in radial astrocytes. Ca^{2+} signal, averaged over fish and trials, reflects P, the probability that a swim bout gives visual feedback, so glia accumulate information on swim futility over time (n = 14 fish).

(L) Circuit diagram. NE-MO represents mismatch signal, computed from visual and motor efference input. Noradrenergic axons from NE-MO excite glial processes in L-MO through α1B NE receptors (see Figure S6C for projections). Radial astrocytes integrate mismatch signals and suppress swimming via downstream GABAergic neurons.

In the hippocampus, astrocytes can be intermediates between cholinergic input and interneurons (Pabst et al., 2016). Glial cells in zebrafish are activated before and during generalized seizures (Verdugo et al., 2019). These and other studies (Adamsky et al., 2018; Ding et al., 2013; Paukert et al., 2014; Poskanzer and Yuste, 2016; Srinivasan et al., 2015) point to an integrated role for astrocytes in information processing in brain circuits.

Our study establishes radial astrocytes as essential computational elements in a circuit that mediates an adaptive behavioral response. The algorithm implemented by the radial astrocytes here is surprisingly analogous to that observed in mouse

hippocampal slices (Deemyad et al., 2018). There, astrocytes integrate neural signals over many seconds and then suddenly switch into a mode where they drive strong inhibition. This "integrate and suppress" functional motif may therefore generalize across neural systems and species. Interestingly, a role for astrocytes in regulating active and passive states of circuits, albeit in a mechanistically different form and on a longer timescale, was conjectured a century ago (Ramon y Cajal, 1895).

How do radial astrocytes drive activity in GABAergic edge cells? Astrocytes can influence synaptic transmission and neuronal firing in multiple ways (Bazargani and Attwell, 2016), but it is unclear which mechanisms are most relevant *in vivo* (Fiacco and McCarthy, 2018; Savtchouk and Volterra, 2018). In *Drosophila*, astrocytes inhibit downstream neurons likely through ATP secretion to influence chemotaxis and startle behavior (Ma et al., 2016). Astrocytes can release GABA (Angulo et al., 2008; Lee et al., 2010; Christensen et al., 2018). They can also influence neuronal firing by modulating extracellular ionic composition. On slow timescales, astrocytes affect neuronal firing via changes in the density of inward-rectifying K^+ membrane channels during depression in rodents (Cui et al., 2018). On faster timescales, glia-like support cells in the developing cochlea trigger neural activity in adjacent hair cells by modulating extracellular K^+ through a calcium-activated chloride channel (Wang et al., 2015). Our study shows that radial astrocytes modulate neurons and influence behavior over seconds (likely triggered by intracellular Ca^{2+} signaling, but possibly via other second messenger systems). The molecular mechanisms were not identified, but may include active control of extracellular ion concentrations near the GABAergic neurons. Radial astrocytes may affect behavior through more pathways than only the GABAergic L-MO cells. Other routes may exist between the glial cells and other neuron types, potentially including direct suppressive effects (Christensen et al., 2018; Wang et al., 2012) on premotor neurons.

Homology between radial astrocytes in zebrafish and astrocytes in mammals is suggested by several similarities. Both cell types have a bushy morphology, which in zebrafish appears after intense neurogenesis (2–3 days post fertilization [David Lyons, personal communication]), qualitatively similar to the emergence of bushy processes when mammalian radial glia convert to astrocytes at the end of embryonic development (Kriegstein and Alvarez-Buylla, 2009). We also found that fish radial astrocytes integrate norepinephrine with local circuit activity, similar to astrocytes in mammalian cortex (Paukert et al., 2014). These findings, in combination with overlapping gene expression and morphological features (Lyons and Talbot, 2014), suggest that the mechanisms shown here may be relevant for neuron-astrocyte interactions and glial control of behavior in other vertebrates.

Neuronal manipulation experiments come with caveats (Otchy et al., 2015); glial manipulation experiments come with more (see Table S1), in part because tools for manipulating glia are less established. Thus, we did six experiments to activate or silence radial astrocytes, attempting to falsify our emerging model that astrocytic activation halts swimming in futility-induced passivity. All six support a causal role for glia in triggering passivity.

Our finding that the NE system encodes the magnitude of failure is consistent with noradrenergic neurons encoding changes in relationships between actions and outcomes (Aston-Jones and Cohen, 2005; Bouret and Sara, 2004; Sara, 2009; Tervo et al., 2014). NE also encodes alertness in zebrafish (Lovett-Barron et al., 2017), which may correlate to the temporary increase in swim vigor after actions become ineffective.

Different action-outcome contingencies lead to different behaviors. When desired outcomes are attainable, motor learning fine-tunes actions; when they are unattainable, futility-induced passivity interrupts behavior. The serotonergic system mediates a form of motor learning in zebrafish by integrating backward visual flow during swimming (Kawashima et al., 2016). Thus, multiple neuromodulatory systems underlie complementary adaptive strategies: the serotonergic system encodes the degree of success of actions and leads to fine-tuning of swim vigor, while the noradrenergic system encodes failure and can drive passivity.

Futility-induced passivity belongs to a class of behaviors in which motor output is reduced, including learned helplessness (Maier, 1984), passive coping (Andalman et al., 2019; Warden et al., 2012), feigned death (Humphreys and Ruxton, 2018), and break-point behavior, where attempts to achieve reward are abandoned (Salamone et al., 2016). Although the behavior studied here is mediated by cells in the brainstem, this broader class of behaviors can involve other brain regions in mammals, including multiple neuromodulatory systems and cortical areas (Roseberry and Kreitzer, 2017).

Evidence-accumulation signals have been found in neuronal firing rates in multiple decision-making paradigms (Scott et al., 2017; Shadlen and Newsome, 2001). Here, we found that, following a switch from a closed-loop to a stochastic feedback protocol, calcium levels in radial astrocytes reflect evidence that actions are futile. The intracellular messengers in the pathway from NE receptors to intracellular Ca^{2+} increases may also be involved in the accumulation process. It remains to be elucidated which of these molecules gets thresholded (and how) to mediate the "decision" to trigger passivity.

We ascribe evidence accumulation to radial astrocytes and sensory-motor-mismatch encoding to NE-MO, but the boundary between the two operations may not be strict. NE-MO may take part in the accumulation, for example over shorter timescales or during the first few swim failures.

What class of computations might astrocytes support? In addition to having different inputs from neurons, these cell types may be specialized for different input-output transformations, based on their spatiotemporal dynamics. Neurons convert chemical inputs into membrane voltage, electrically integrate across thousands of such inputs, and fire action potentials in milliseconds. Although glial processes can respond to neurons in ~100 ms (Stobart et al., 2018), glia often operate on slower timescales using molecular signaling. Such properties may favor astrocytes for computations involving slow integration of activity. The molecular mechanisms of astrocytic computation are not yet clear, and understanding their spatial interactions with neurons may require incorporating astrocytes into electron microscopy-based circuit reconstruction (Briggman and Bock, 2012). Broadening such efforts to include astrocytes will likely accelerate neuroscience discovery.

STAR★METHODS

Detailed methods are provided in the online version of this paper and include the following:

- KEY RESOURCES TABLE
- LEAD CONTACT AND MATERIALS AVAILABILITY
- EXPERIMENTAL MODEL AND SUBJECT DETAILS
  - Zebrafish
  - Transgenesis
- METHOD DETAILS
  - Preparation for fictive-behavior assays
  - Fictive behavior in virtual reality
  - Futility-induced passivity behavioral analysis
  - DMD-based optogenetic stimulation
  - Two-photon ablation of cells
  - Forebrain lesioning
  - TRPV1-mediated activation of radial astrocytes
  - IP_3 receptor blockade
  - Analysis of fluorescence imaging data
  - Confocal microscopy
  - Single-cell radial astrocyte tracing
  - *In situ* hybridization
  - Immunohistochemistry with expansion microscopy
  - RNA sequencing
- DATA AND CODE AVAILABILITY

SUPPLEMENTAL INFORMATION

Supplemental Information can be found online at https://doi.org/10.1016/j.cell.2019.05.050.

A video abstract is available at https://doi.org/10.1016/j.cell.2019.05.050#mmc11.

ACKNOWLEDGMENTS

We thank C. Wang, P. Keller, and T. Kawashima for help with optics; A. Lemire and L. Wang for help with transcriptomics; P. Tillberg and A. Hu for help with anatomy imaging and tissue expansion; M. Copeland for help with *in situ* hybridization; M. Koyama for help with electrophysiology infrastructure; I. Bianco, H. Burgess, and D. Lyons for suggestions; M. Koyama, N. Spruston, D. Bergles, J. Du, J. Lippincott-Schwartz, J. Freeman, J. Wittenbach, D. Wolpert, J. Dudman, M. Hale, E. Yaksi, C. Brody, F. Engert, K. Monk, M. Hatten, B. Khakh, Y. Liao, and C. Zuker for discussions; V. Jayaraman, N. Li, A. Lee, U. Heberlein, W. Ge, Y. Wang, J. Phillips, S. Chen, D. Stern, D. Lyons, D. Schoppik, S. Liddelow, M. Warden, and S. Chen for comments on the paper; J. Rouchard, J. Cox and vivarium staff for fish husbandry and help making transgenic fish; D. Prober for the TRPV1 gene; P. Raymond for the *gfap* promoter; and E. Boyden for the CoChR gene. This work was supported by the Howard Hughes Medical Institute and Simons Collaboration on the Global Brain Awards (325171, 542943SPI).

AUTHOR CONTRIBUTIONS

Y.M., D.V.B., M.R., S.N., and M.B.A. conceived the project. Y.M., D.V.B., and S.N. performed the experiments. M.R. created the analysis pipeline. M.R., Y.M., and D.V.B. analyzed the data. D.V.B. built the optical excitation setup. S.N. and C.-T.Y. generated transgenic fish. M.T. and Y.M. did glial electrophysiology. L.L.L. analyzed RNA-seq data. M.B.A. supervised the study. Y.M., D.B., M.R., B.D.M., and M.B.A. wrote the paper.

DECLARATION OF INTERESTS

The authors declare no competing interests.

Received: October 3, 2018
Revised: January 31, 2019
Accepted: May 23, 2019
Published: June 20, 2019

REFERENCES

Adamsky, A., Kol, A., Kreisel, T., Doron, A., Ozeri-Engelhard, N., Melcer, T., Refaeli, R., Horn, H., Regev, L., Groysman, M., et al. (2018). Astrocytic Activation Generates De Novo Neuronal Potentiation and Memory Enhancement. Cell *174*, 59–71.e14.

Ahrens, M.B., Li, J.M., Orger, M.B., Robson, D.N., Schier, A.F., Engert, F., and Portugues, R. (2012). Brain-wide neuronal dynamics during motor adaptation in zebrafish. Nature *485*, 471–477.

Ahrens, M.B., Orger, M.B., Robson, D.N., Li, J.M., and Keller, P.J. (2013). Whole-brain functional imaging at cellular resolution using light-sheet microscopy. Nat. Methods *10*, 413–420.

Airan, R.D., Thompson, K.R., Fenno, L.E., Bernstein, H., and Deisseroth, K. (2009). Temporally precise in vivo control of intracellular signalling. Nature *458*, 1025–1029.

Andalman, A.S., Burns, V.M., Lovett-Barron, M., Broxton, M., Poole, B., Yang, S.J., Grosenick, L., Lerner, T.N., Chen, R., Benster, T., et al. (2019). Neuronal Dynamics Regulating Brain and Behavioral State Transitions. Cell *177*, 970–985.e20.

Angulo, M.C., Le Meur, K., Kozlov, A.S., Charpak, S., and Audinat, E. (2008). GABA, a forgotten gliotransmitter. Prog. Neurobiol. *86*, 297–303.

Anthony, T.E., Klein, C., Fishell, G., and Heintz, N. (2004). Radial glia serve as neuronal progenitors in all regions of the central nervous system. Neuron *41*, 881–890.

Araque, A., Carmignoto, G., Haydon, P.G., Oliet, S.H.R., Robitaille, R., and Volterra, A. (2014). Gliotransmitters travel in time and space. Neuron *81*, 728–739.

Aston-Jones, G., and Cohen, J.D. (2005). An integrative theory of locus coeruleus-norepinephrine function: adaptive gain and optimal performance. Annu Rev Neurosci. *28*, 403–450.

Avants, B.B., Yushkevich, P., Pluta, J., Minkoff, D., Korczykowski, M., Detre, J., and Gee, J.C. (2010). The optimal template effect in hippocampus studies of diseased populations. Neuroimage *49*, 2457–2466.

Banker, G.A. (1980). Trophic interactions between astroglial cells and hippocampal neurons in culture. Science *209*, 809–810.

Barres, B.A. (2008). The mystery and magic of glia: a perspective on their roles in health and disease. Neuron *60*, 430–440.

Bazargani, N., and Attwell, D. (2016). Astrocyte calcium signaling: the third wave. Nat. Neurosci. *19*, 182–189.

Bekar, L.K., He, W., and Nedergaard, M. (2008). Locus coeruleus α-adrenergic-mediated activation of cortical astrocytes in vivo. Cereb. Cortex *18*, 2789–2795.

Bernardos, R.L., and Raymond, P.A. (2006). GFAP transgenic zebrafish. Gene Expr. Patterns *6*, 1007–1013.

Berry, M.W., Browne, M., Langville, A.N., Pauca, V.P., and Plemmons, R.J. (2007). Algorithms and applications for approximate nonnegative matrix factorization. Comput. Stat. Data Anal. *52*, 155–173.

Bouret, S., and Sara, S.J. (2004). Reward expectation, orientation of attention and locus coeruleus-medial frontal cortex interplay during learning. Eur. J. Neurosci. *20*, 791–802.

Boutsidis, C., and Gallopoulos, E. (2008). SVD based initialization: A head start for nonnegative matrix factorization. Pattern Recognit. *41*, 1350–1362.

Briggman, K.L., and Bock, D.D. (2012). Volume electron microscopy for neuronal circuit reconstruction. Curr. Opin. Neurobiol. *22*, 154–161.

Cembrowski, M.S., Wang, L., Sugino, K., Shields, B.C., and Spruston, N. (2016). Hipposeq: a comprehensive RNA-seq database of gene expression in hippocampal principal neurons. eLife *5*, e14997.

Chen, T.-W., Wardill, T.J., Sun, Y., Pulver, S.R., Renninger, S.L., Baohan, A., Schreiter, E.R., Kerr, R.A., Orger, M.B., Jayaraman, V., et al. (2013). Ultrasensitive fluorescent proteins for imaging neuronal activity. Nature *499*, 295–300.

Chen, S., Chiu, C.N., McArthur, K.L., Fetcho, J.R., and Prober, D.A. (2016). TRP channel mediated neuronal activation and ablation in freely behaving zebrafish. Nat. Methods *13*, 147–150.

Christensen, R.K., Delgado-Lezama, R., Russo, R.E., Lind, B.L., Alcocer, E.L., Rath, M.F., Fabbiani, G., Schmitt, N., Lauritzen, M., Petersen, A.V., et al. (2018). Spinal dorsal horn astrocytes release GABA in response to synaptic activation. J. Physiol. *596*, 4983–4994.

Cui, Y., Yang, Y., Ni, Z., Dong, Y., Cai, G., Foncelle, A., Ma, S., Sang, K., Tang, S., Li, Y., et al. (2018). Astroglial Kir4.1 in the lateral habenula drives neuronal bursts in depression. Nature *554*, 323–327.

Cuoghi, B., and Mola, L. (2009). Macroglial cells of the teleost central nervous system: a survey of the main types. Cell Tissue Res. *338*, 319–332.

Dana, H., Mohar, B., Sun, Y., Narayan, S., Gordus, A., Hasseman, J.P., Tsegaye, G., Holt, G.T., Hu, A., Walpita, D., et al. (2016). Sensitive red protein calcium indicators for imaging neural activity. eLife *5*, e12727.

Deemyad, T., Lüthi, J., and Spruston, N. (2018). Astrocytes integrate and drive action potential firing in inhibitory subnetworks. Nat. Commun. *9*, 4336.

Ding, F., O'Donnell, J., Thrane, A.S., Zeppenfeld, D., Kang, H., Xie, L., Wang, F., and Nedergaard, M. (2013). α1-Adrenergic receptors mediate coordinated Ca2+ signaling of cortical astrocytes in awake, behaving mice. Cell Calcium *54*, 387–394.

Dunn, T.W., Mu, Y., Narayan, S., Randlett, O., Naumann, E.A., Yang, C.-T., Schier, A.F., Freeman, J., Engert, F., and Ahrens, M.B. (2016). Brain-wide mapping of neural activity controlling zebrafish exploratory locomotion. eLife *5*, e12741.

Farrar, M.J., Kolkman, K.E., and Fetcho, J.R. (2018). Features of the structure, development, and activity of the zebrafish noradrenergic system explored in new CRISPR transgenic lines. J. Comp. Neurol. *526*, 2493–2508.

Fiacco, T.A., and McCarthy, K.D. (2018). Multiple Lines of Evidence Indicate That Gliotransmission Does Not Occur under Physiological Conditions. J. Neurosci. *38*, 3–13.

Figueiredo, M., Lane, S., Stout, R.F., Jr., Liu, B., Parpura, V., Teschemacher, A.G., and Kasparov, S. (2014). Comparative analysis of optogenetic actuators in cultured astrocytes. Cell Calcium *56*, 208–214.

Freeman, J., Vladimirov, N., Kawashima, T., Mu, Y., Sofroniew, N.J., Bennett, D.V., Rosen, J., Yang, C.-T., Looger, L.L., and Ahrens, M.B. (2014). Mapping brain activity at scale with cluster computing. Nat. Methods *11*, 941–950.

Freifeld, L., Odstrcil, I., Förster, D., Ramirez, A., Gagnon, J.A., Randlett, O., Costa, E.K., Asano, S., Celiker, O.T., Gao, R., et al. (2017). Expansion microscopy of zebrafish for neuroscience and developmental biology studies. Proc. Natl. Acad. Sci. USA *114*, E10799–E10808.

Fujii, Y., Maekawa, S., and Morita, M. (2017). Astrocyte calcium waves propagate proximally by gap junction and distally by extracellular diffusion of ATP released from volume-regulated anion channels. Sci. Rep. *7*, 13115.

Fujita, T., Chen, M.J., Li, B., Smith, N.A., Peng, W., Sun, W., Toner, M.J., Kress, B.T., Wang, L., Benraiss, A., et al. (2014). Neuronal transgene expression in dominant-negative SNARE mice. J. Neurosci. *34*, 16594–16604.

Gafni, J., Munsch, J.A., Lam, T.H., Catlin, M.C., Costa, L.G., Molinski, T.F., and Pessah, I.N. (1997). Xestospongins: potent membrane permeable blockers of the inositol 1,4,5-trisphosphate receptor. Neuron *19*, 723–733.

Gourine, A.V., Kasymov, V., Marina, N., Tang, F., Figueiredo, M.F., Lane, S., Teschemacher, A.G., Spyer, K.M., Deisseroth, K., and Kasparov, S. (2010). Astrocytes control breathing through pH-dependent release of ATP. Science *329*, 571–575.

Gross-Thebing, T., Paksa, A., and Raz, E. (2014). Simultaneous high-resolution detection of multiple transcripts combined with localization of proteins in whole-mount embryos. BMC Biol. *12*, 55.

Grupp, L., Wolburg, H., and Mack, A.F. (2010). Astroglial structures in the zebrafish brain. J. Comp. Neurol. *518*, 4277–4287.

Haydon, P.G., and Nedergaard, M. (2014). How do astrocytes participate in neural plasticity? Cold Spring Harb. Perspect. Biol. *7*, a020438.

Hempel, C.M., Sugino, K., and Nelson, S.B. (2007). A manual method for the purification of fluorescently labeled neurons from the mammalian brain. Nat. Protoc. *2*, 2924–2929.

Hoyer, P.O. (2004). Non-negative matrix factorization with sparseness constraints. J. Mach. Learn. Res. *5*, 1457–1469.

Humphreys, R.K., and Ruxton, G.D. (2018). A review of thanatosis (death feigning) as an anti-predator behaviour. Behav. Ecol. Sociobiol. (Print) *72*, 22.

Kawashima, T., Zwart, M.F., Yang, C.-T., Mensh, B.D., and Ahrens, M.B. (2016). The Serotonergic System Tracks the Outcomes of Actions to Mediate Short-Term Motor Learning. Cell *167*, 933–946.e20.

Keller, G.B., Bonhoeffer, T., and Hübener, M. (2012). Sensorimotor mismatch signals in primary visual cortex of the behaving mouse. Neuron *74*, 809–815.

Kimura, Y., Hisano, Y., Kawahara, A., and Higashijima, S. (2014). Efficient generation of knock-in transgenic zebrafish carrying reporter/driver genes by CRISPR/Cas9-mediated genome engineering. Sci. Rep. *4*, 6545.

Kjaerby, C., Rasmussen, R., Andersen, M., and Nedergaard, M. (2017). Does Global Astrocytic Calcium Signaling Participate in Awake Brain State Transitions and Neuronal Circuit Function? Neurochem. Res. *42*, 1810–1822.

Klapoetke, N.C., Murata, Y., Kim, S.S., Pulver, S.R., Birdsey-Benson, A., Cho, Y.K., Morimoto, T.K., Chuong, A.S., Carpenter, E.J., Tian, Z., et al. (2014). Independent optical excitation of distinct neural populations. Nat. Methods *11*, 338–346.

Koyama, M., Kinkhabwala, A., Satou, C., Higashijima, S., and Fetcho, J. (2011). Mapping a sensory-motor network onto a structural and functional ground plan in the hindbrain. Proc Natl Acad Sci USA *108*, 1170–1175.

Kriegstein, A., and Alvarez-Buylla, A. (2009). The glial nature of embryonic and adult neural stem cells. Annu. Rev. Neurosci. *32*, 149–184.

Lee, S., Yoon, B.-E., Berglund, K., Oh, S.-J., Park, H., Shin, H.-S., Augustine, G.J., and Lee, C.J. (2010). Channel-mediated tonic GABA release from glia. Science *330*, 790–796.

Li, J., Zhang, B.B., Ren, Y.G., Gu, S.Y., Xiang, Y.H., and Du, J.L. (2015). Intron targeting-mediated and endogenous gene integrity-maintaining knockin in zebrafish using the CRISPR/Cas9 system. Cell Res. *25*, 634–637.

Liao, J.C., and Fetcho, J.R. (2008). Shared versus specialized glycinergic spinal interneurons in axial motor circuits of larval zebrafish. J. Neurosci. *28*, 12982–12992.

Lovett-Barron, M., Andalman, A.S., Allen, W.E., Vesuna, S., Kauvar, I., Burns, V.M., and Deisseroth, K. (2017). Ancestral Circuits for the Coordinated Modulation of Brain State. Cell *171*, 1411–1423.e17.

Lyons, D.A., and Talbot, W.S. (2014). Glial cell development and function in zebrafish. Cold Spring Harb. Perspect. Biol. *7*, a020586.

Ma, Z., Stork, T., Bergles, D.E., and Freeman, M.R. (2016). Neuromodulators signal through astrocytes to alter neural circuit activity and behaviour. Nature *539*, 428–432.

Maier, S.F. (1984). Learned helplessness and animal models of depression. Prog. Neuropsychopharmacol. Biol. Psychiatry *8*, 435–446.

Marquart, G.D., Tabor, K.M., Brown, M., Strykowski, J.L., Varshney, G.K., LaFave, M.C., Mueller, T., Burgess, S.M., Higashijima, S., and Burgess, H.A. (2015). A 3D Searchable Database of Transgenic Zebrafish Gal4 and Cre Lines for Functional Neuroanatomy Studies. Front. Neural Circuits *9*, 78.

Morquette, P., Verdier, D., Kadala, A., Féthière, J., Philippe, A.G., Robitaille, R., and Kolta, A. (2015). An astrocyte-dependent mechanism for neuronal rhythmogenesis. Nat. Neurosci. *18*, 844–854.

Munns, C.H., Chung, M.-K., Sanchez, Y.E., Amzel, L.M., and Caterina, M.J. (2015). Role of the outer pore domain in transient receptor potential vanilloid 1 dynamic permeability to large cations. J. Biol. Chem. *290*, 5707–5724.

Nedergaard, M. (1994). Direct signaling from astrocytes to neurons in cultures of mammalian brain cells. Science *263*, 1768–1771.

Orger, M.B., Smear, M.C., Anstis, S.M., and Baier, H. (2000). Perception of Fourier and non-Fourier motion by larval zebrafish. Nat. Neurosci. *3*, 1128–1133.

Otchy, T.M., Wolff, S.B.E., Rhee, J.Y., Pehlevan, C., Kawai, R., Kempf, A., Gobes, S.M.H., and Ölveczky, B.P. (2015). Acute off-target effects of neural circuit manipulations. Nature *528*, 358–363.

Pabst, M., Braganza, O., Dannenberg, H., Hu, W., Pothmann, L., Rosen, J., Mody, I., van Loo, K., Deisseroth, K., Becker, A.J., et al. (2016). Astrocyte Intermediaries of Septal Cholinergic Modulation in the Hippocampus. Neuron *90*, 853–865.

Palla, G., Derényi, I., Farkas, I., and Vicsek, T. (2005). Uncovering the overlapping community structure of complex networks in nature and society. Nature *435*, 814–818.

Panier, T., Romano, S.A., Olive, R., Pietri, T., Sumbre, G., Candelier, R., and Debrégeas, G. (2013). Fast functional imaging of multiple brain regions in intact zebrafish larvae using selective plane illumination microscopy. Front. Neural Circuits *7*, 65.

Park, H.C., Kim, C.H., Bae, Y.K., Yeo, S.Y., Kim, S.H., Hong, S.K., Shin, J., Yoo, K.W., Hibi, M., Hirano, T., et al. (2000). Analysis of upstream elements in the HuC promoter leads to the establishment of transgenic zebrafish with fluorescent neurons. Dev. Biol. *227*, 279–293.

Parpura, V., Basarsky, T.A., Liu, F., Jeftinija, K., Jeftinija, S., and Haydon, P.G. (1994). Glutamate-mediated astrocyte-neuron signalling. Nature *369*, 744–747.

Paukert, M., Agarwal, A., Cha, J., Doze, V.A., Kang, J.U., and Bergles, D.E. (2014). Norepinephrine controls astroglial responsiveness to local circuit activity. Neuron *82*, 1263–1270.

Pinto, L., Koay, S.A., Engelhard, B., Yoon, A.M., Deverett, B., Thiberge, S.Y., Witten, I.B., Tank, D.W., and Brody, C.D. (2018). An Accumulation-of-Evidence Task Using Visual Pulses for Mice Navigating in Virtual Reality. Front. Behav. Neurosci. *12*, 36.

Portugues, R., and Engert, F. (2011). Adaptive locomotor behavior in larval zebrafish. Front. Syst. Neurosci. *5*, 72.

Poskanzer, K.E., and Yuste, R. (2016). Astrocytes regulate cortical state switching in vivo. Proc. Natl. Acad. Sci. USA *113*, E2675–E2684.

Ramon y Cajal, S. (1895). Algunas conjeturas sobre el mecanismo anatómico de la ideación, asociación y atención. Rev. Med. Cir. Pract. *36*, 497–508.

Randlett, O., Wee, C.L., Naumann, E.A., Nnaemeka, O., Schoppik, D., Fitzgerald, J.E., Portugues, R., Lacoste, A.M.B., Riegler, C., Engert, F., and Schier, A.F. (2015). Whole-brain activity mapping onto a zebrafish brain atlas. Nat. Methods *12*, 1039–1046.

Rinaman, L. (2011). Hindbrain noradrenergic A2 neurons: diverse roles in autonomic, endocrine, cognitive, and behavioral functions. Am. J. Physiol. Regul. Integr. Comp. Physiol. *300*, R222–R235.

Rock, I., and Smith, D. (1986). The optomotor response and induced motion of the self. Perception *15*, 497–502.

Roseberry, T., and Kreitzer, A. (2017). Neural circuitry for behavioural arrest. Philos. Trans. R. Soc. B Biol. Sci. *372*, 20160197.

Salamone, J.D., Correa, M., Yohn, S., Lopez Cruz, L., San Miguel, N., and Alatorre, L. (2016). The pharmacology of effort-related choice behavior: Dopamine, depression, and individual differences. Behav. Processes *127*, 3–17.

Sanz-Salvador, L., Andrés-Borderia, A., Ferrer-Montiel, A., and Planells-Cases, R. (2012). Agonist- and Ca2+-dependent desensitization of TRPV1 channel targets the receptor to lysosomes for degradation. J. Biol. Chem. *287*, 19462–19471.

Sara, S.J. (2009). The locus coeruleus and noradrenergic modulation of cognition. Nat. Rev. Neurosci. *10*, 211–223.

Satou, C., Kimura, Y., Hirata, H., Suster, M.L., Kawakami, K., and Higashijima, S. (2013). Transgenic tools to characterize neuronal properties of discrete populations of zebrafish neurons. Development *140*, 3927–3931.

Savtchouk, I., and Volterra, A. (2018). Gliotransmission: Beyond Black-and-White. J. Neurosci. *38*, 14–25.

Schummers, J., Yu, H., and Sur, M. (2008). Tuned responses of astrocytes and their influence on hemodynamic signals in the visual cortex. Science *320*, 1638–1643.

Scott, B.B., Constantinople, C.M., Akrami, A., Hanks, T.D., Brody, C.D., and Tank, D.W. (2017). Fronto-parietal Cortical Circuits Encode Accumulated Evidence with a Diversity of Timescales. Neuron *95*, 385–398.e5.

Shadlen, M.N., and Newsome, W.T. (2001). Neural basis of a perceptual decision in the parietal cortex (area LIP) of the rhesus monkey. J. Neurophysiol. *86*, 1916–1936.

Slezak, M., Kandler, S., Van Veldhoven, P.P., Bonin, V., and Holt, M.G. (2018). Astrocytes integrate local sensory and brain-wide neuromodulatory signals. bioRxiv. https://doi.org/10.1101/381434.

Sloan, S.A., and Barres, B.A. (2014). Looks can be deceiving: reconsidering the evidence for gliotransmission. Neuron *84*, 1112–1115.

Srinivasan, R., Huang, B.S., Venugopal, S., Johnston, A.D., Chai, H., Zeng, H., Golshani, P., and Khakh, B.S. (2015). Ca(2+) signaling in astrocytes from Ip3r2(-/-) mice in brain slices and during startle responses in vivo. Nat. Neurosci. *18*, 708–717.

Stobart, J.L., Ferrari, K.D., Barrett, M.J.P., Glück, C., Stobart, M.J., Zuend, M., and Weber, B. (2018). Cortical Circuit Activity Evokes Rapid Astrocyte Calcium Signals on a Similar Timescale to Neurons. Neuron *98*, 726–735.e4.

Tabor, K.M., Bergeron, S.A., Horstick, E.J., Jordan, D.C., Aho, V., Porkka-Heiskanen, T., Haspel, G., and Burgess, H.A. (2014). Direct activation of the Mauthner cell by electric field pulses drives ultrarapid escape responses. J. Neurophysiol. *112*, 834–844.

Tay, T.L., Ronneberger, O., Ryu, S., Nitschke, R., and Driever, W. (2011). Comprehensive catecholaminergic projectome analysis reveals single-neuron integration of zebrafish ascending and descending dopaminergic systems. Nat. Commun. *2*, 171.

Tervo, D.G.R., Proskurin, M., Manakov, M., Kabra, M., Vollmer, A., Branson, K., and Karpova, A.Y. (2014). Behavioral variability through stochastic choice and its gating by anterior cingulate cortex. Cell *159*, 21–32.

Tillberg, P.W., Chen, F., Piatkevich, K.D., Zhao, Y., Yu, C.-C.J., English, B.P., Gao, L., Martorell, A., Suk, H.-J., Yoshida, F., et al. (2016). Protein-retention expansion microscopy of cells and tissues labeled using standard fluorescent proteins and antibodies. Nat. Biotechnol. *34*, 987–992.

Uchida, D., Yamashita, M., Kitano, T., and Iguchi, T. (2002). Oocyte apoptosis during the transition from ovary-like tissue to testes during sex differentiation of juvenile zebrafish. J. Exp. Biol. *205*, 711–718.

Urasaki, A. (2009). Analysis of genes and genome by the tol2-mediated gene and enhancer trap methods. Methods Mol Biol. *546*, 85–102.

Verdugo, C.D., Myren-Svelstad, S., Deneubourg, C., Pelgrims, R., Muto, A., Kawakami, K., Jurisch-Yaksi, N., and Yaksi, E. (2019). Glia-neuron interactions underlie state transitions to generalized seizures. bioRxiv. https://doi.org/10.1101/509521.

Verkhratsky, A., Orkand, R.K., and Kettenmann, H. (1998). Glial calcium: homeostasis and signaling function. Physiol. Rev. *78*, 99–141.

Vladimirov, N., Mu, Y., Kawashima, T., Bennett, D.V., Yang, C.-T., Looger, L.L., Keller, P.J., Freeman, J., and Ahrens, M.B. (2014). Light-sheet functional imaging in fictively behaving zebrafish. Nat. Methods *11*, 883–884.

Vladimirov, N., Wang, C., Höckendorf, B., Pujala, A., Tanimoto, M., Mu, Y., Yang, C.-T., Wittenbach, J.D., Freeman, J., Preibisch, S., et al. (2018). Brain-wide circuit interrogation at the cellular level guided by online analysis of neuronal function. Nat. Methods *15*, 1117–1125.

Wang, F., Smith, N.A., Xu, Q., Fujita, T., Baba, A., Matsuda, T., Takano, T., Bekar, L., and Nedergaard, M. (2012). Astrocytes modulate neural network activity by Ca^2+-dependent uptake of extracellular K+. Sci. Signal. *5*, ra26.

Wang, H.C., Lin, C.-C., Cheung, R., Zhang-Hooks, Y., Agarwal, A., Ellis-Davies, G., Rock, J., and Bergles, D.E. (2015). Spontaneous Activity of Cochlear Hair Cells Triggered by Fluid Secretion Mechanism in Adjacent Support Cells. Cell *163*, 1348–1359.

Warden, M.R., Selimbeyoglu, A., Mirzabekov, J.J., Lo, M., Thompson, K.R., Kim, S.-Y., Adhikari, A., Tye, K.M., Frank, L.M., and Deisseroth, K. (2012).

A prefrontal cortex-brainstem neuronal projection that controls response to behavioural challenge. Nature *492*, 428–432.

Westerfield, M. (2007). A Guide for the Laboratory Use of Zebrafish (Danio Rerio).

White, R.M., Sessa, A., Burke, C., Bowman, T., LeBlanc, J., Ceol, C., Bourque, C., Dovey, M., Goessling, W., Burns, C.E., and Zon, L.I. (2008). Transparent adult zebrafish as a tool for in vivo transplantation analysis. Cell Stem Cell *2*, 183–189.

Yu, X., Taylor, A.M.W., Nagai, J., Golshani, P., Evans, C.J., Coppola, G., and Khakh, B.S. (2018). Reducing Astrocyte Calcium Signaling In Vivo Alters Striatal Microcircuits and Causes Repetitive Behavior. Neuron *99*, 1170–1187.e9.

Zaharia, M., Chowdhury, M., Franklin, M.J., Shenker, S., and Stoica, I. (2010). Spark: Cluster computing with working sets. Proceedings of the 2nd USENIX Conference on Hot Topics in Cloud Computing *10*.

Zhu, P., Fajardo, O., Shum, J., Zhang Schärer, Y.-P., and Friedrich, R.W. (2012a). High-resolution optical control of spatiotemporal neuronal activity patterns in zebrafish using a digital micromirror device. Nat. Protoc. *7*, 1410–1425.

Zhu, S., Lee, J.-S., Guo, F., Shin, J., Perez-Atayde, A.R., Kutok, J.L., Rodig, S.J., Neuberg, D.S., Helman, D., Feng, H., et al. (2012b). Activated ALK collaborates with MYCN in neuroblastoma pathogenesis. Cancer Cell *21*, 362–373.

STAR★METHODS

KEY RESOURCES TABLE

REAGENT or RESOURCE	SOURCE	IDENTIFIER
Antibodies		
anti-α2B- adrenergic receptor	Life Technologies	Cat# MA1-12721; RRID:AB_2225066
Bacterial and Virus Strains		
dbh-GFP-pDEST-ISce	(Zhu et al., 2012b)	N/A
FCK-gene86-GFP (CoChR)	(Klapoetke et al., 2014)	N/A
(Tol2-Isl-gal4vp16-4; UAS:TrpV1-tagRFpt)	(Chen et al., 2016)	N/A
pEGFP-gfap (Intron1/5′/Exon1-zebrafish)	Addgene	Cat# 39761
pcDNA3.1-opto-α1AR-EYFP	Addgene	Cat# 20947
Experimental Models: Organisms/Strains		
Tg(elavl3:GCaMP6f)^{jf1}	Janelia Research Campus (JRC) (Freeman et al., 2014)	N/A
Tg(elavl3:jRGECO1b)^{jf17}	JRC (Dana et al., 2016)	N/A
Tg(elavl3:H2B-GCaMP6f)^{jf7}	JRC (Dunn et al., 2016)	N/A
Tg(gfap:jRGECO1b)^{jf33}	JRC	N/A
Tg(gfap:GCaMP6f)^{jf22}	JRC	N/A
Tg(gfap:CoChR-eGFP)^{jf29}	JRC	N/A
Tg(gfap:opto-α1AR-eYFP)^{jf81}	JRC	N/A
Tg(gfap:H2B-GCaMP6f)^{jf23}	JRC	N/A
Tg(dbh:KalTA4)^{jf12}	JRC	N/A
Tg(UAS:CoChR-eGFP)^{jf44}	JRC	N/A
Tg(gfap:tdTomato)^{jf21}	JRC	N/A
Tg(gad1b:Gal4)^{jf49}	JRC	N/A
Tg(th-P2A-Gal4)	Chinese Academy of Sciences (Li et al., 2015)	N/A
Tg(UAS:GCaMP6s)	National Institute of Genetics	N/A
Tg(net:mTdTomato)	Cornell University (Farrar et al., 2018)	N/A
Tg(net:H2B-GCaMP6f)	Cornell University (Farrar et al., 2018)	N/A
Tg(gad1b:loxP-RFP-loxP-GFP)	Okazaki Institute for Integrative Bioscience (Satou et al., 2013)	N/A
Software and Algorithms		
MATLAB	MathWorks	https://www.mathworks.com
ImageJ	National Institutes of Health	https://imagej.nih.gov/ij/
C# (.NET Framework 3.5) (stimulus/behavior)	Microsoft	https://docs.microsoft.com/en-us/dotnet/csharp/
Cell segmentation and component detection	This study	https://github.com/mikarubi/segmentation
Chemicals, Peptides, and Recombinant Proteins		
Alpha-Bungarotoxin	Sigma-Aldrich	Cat# B137
Capsaicin	Sigma-Aldrich	Cat# M2028
Xestospongin C	Sigma-Aldrich	Cat# X2628
Prazosin hydrochloride	Sigma-Aldrich	Cat# P7791
Cyclazosin hydrochloride	Sigma-Aldrich	Cat# C247
Idazoxan hydrochloride	Sigma-Aldrich	Cat# I6138
Propranolol hydrochloride	Sigma-Aldrich	Cat# P0884
Methoxamine hydrochloride	Sigma-Aldrich	Cat# M6524

(*Continued on next page*)

Continued

REAGENT or RESOURCE	SOURCE	IDENTIFIER
Dextran, Texas Red	ThermoFisher Scientific	Cat# D3328
Dextran, Fluorescein	ThermoFisher Scientific	Cat# D3306
Metronidazole	MP Biomedicals	Cat# 02155710

LEAD CONTACT AND MATERIALS AVAILABILITY

Information and requests for resources and reagents should be directed to and will be fulfilled by the lead contact Misha B. Ahrens (ahrensm@janelia.hhmi.org).

EXPERIMENTAL MODEL AND SUBJECT DETAILS

Zebrafish

Larvae were reared at 28.5°C in 14:10 light-dark cycles (Westerfield, 2007). Zebrafish from 5 to 7 dpf were fed rotifers and used for experiments. All experiments complied with protocols approved by the Institutional Care and Use Committee at Janelia Research Campus (JRC). Zebrafish sex cannot be determined until ~3 weeks post-fertilization (Uchida et al., 2002), so experimental animals' sex was unknown.

Transgenesis

Transgenic zebrafish larvae were in *casper* or *nacre* background (White et al., 2008). *TgBAC(gad1b:loxP-RFP-loxP-GFP)* (Satou et al., 2013) was used without Cre-mediated recombination and called *Tg(gad1b:RFP)*. *Tg(elavl3:GCaMP6f)*^{jf1}, *Tg(elavl3:H2B-GCaMP6f)*^{jf7}, *Tg(elavl3:ReaChR-TagRFP-T)*^{jf10}, *Tg(elavl3:jRGECO1b)* lines are described (Chen et al., 2013; Dana et al., 2016; Dunn et al., 2016; Vladimirov et al., 2018). *Tg(gfap:jRGECO1b)*, *Tg(gfap:GCaMP6f)*, *Tg(gfap:CoChR-eGFP)*, *Tg(gfap:opto-α1AR-eYFP), Tg(gfap:H2B-GCaMP6f)*, *Tg(dbh:KalTA4)*, *Tg(UAS:CoChR-eGFP)*, and *Tg(gfap:tdTomato)* lines were generated with Tol2 system (Urasaki, 2009), a known gfap promoter sequence (Bernardos and Raymond, 2006) and the following:

1. Construct containing dopamine-β-hydroxylase (dbh) promoter (dbh-GFP-pDEST-ISce); a gift from Thomas Look (Dana Faber Cancer Institute)
2. Construct containing transient receptor potential cation channel subfamily V member 1 (TRPV1) (or capsaicin receptor) from rat; a gift from David Prober (California Institute of Technology)
3. pEGFP-gfap (Intron1/5′/Exon1-zebrafish) (Addgene plasmid # 39761)
4. FCK-gene86-GFP (CoChR); a gift from Ed Boyden (Klapoetke et al., 2014)
5. pcDNA3.1-opto-α1AR-EYFP (Addgene plasmid # 20947)

Tg(gad1b:Gal4) was generated by CRISPR-mediated knock-in of Gal4 (Gal4FF) at gad1b locus as described (Kimura et al., 2014). The sgRNA sequence for gad1b is TGGAACTGCTCACCAGAAGG. 2XNRSE-tbait-hsp70-Gal4 (Kimura et al., 2014) was a gift from Shin-ichi Higashijima.

METHOD DETAILS

Preparation for fictive-behavior assays

All animals in fictive-behavior experiments were paralyzed and restrained. To induce paralysis, we bathed the fish in a 5 mg/mL solution of the nicotinic acetylcholine receptor antagonist α-bungarotoxin for 30 s, then transferred to fish facility water. Once fish no longer responded to tactile stimuli, we transferred them to a plastic Petri dish (for behavioral experiments) or a custom-fabricated sample holder (for light-sheet imaging). Paralyzed fish were then immersed in low-melting point agarose (Sigma) and oriented before it congealed.

Fictive behavior in virtual reality

For fictive swimming and virtual reality (Vladimirov et al., 2014), paralyzed zebrafish were mounted on an acrylic pedestal inside a square water-filled chamber with glass walls and a diffusive screen at the bottom for stimulus projection. Agarose was removed from the head and tail, and large-barrel glass pipettes (~60 μm inner diameter) were attached to the tail with gentle suction. The standard deviation of the left and right motor nerve signal (amplified by a MultiClamp 700B microelectrode amplifier) was calculated in a sliding window of 10 ms: this formed the 'swim signal' or 'swim power' used to quantify behavior.

In closed-loop one-dimensional environments, a stripe pattern (2.5 mm stripe width) was projected underneath the fish by a video projector (MP-CD1, Sony). This pattern moved forward at 2.86 mm/s drift speed when the fish was not swimming. When the fish

swam, the stripe accelerated backward at a rate proportional to swim power, i.e., [stimulus velocity] = [drift speed] – [motosensory gain] × [swim power]. This feedback mimics the visual feedback the animal would receive if it were freely swimming. When [swim power] = 0, forward velocity mimics the fish moving backward (as in a virtual water stream).

In open loop, the gain was zero, so the stripes moved forward at a fixed velocity, independently of whether the fish swam or not.

Brain imaging during fictive behavior used a custom light-sheet microscope, as described (Vladimirov et al., 2014). Briefly, two low-NA laser beams were scanned in the horizontal and vertical planes. The beams entered the chamber through the glass walls. One beam came from the side (relative to the head) and the other from the front of the fish and scanned the area between the eyes. The side laser was switched off at every sweep when pointing at the eye to avoid stimulating the retina. For every horizontal layer sweep, one image was acquired using a 16x/0.8 NA detection objective (Nikon), Nikon tube lens, and a camera (Orca Flash 4.0 v2, Hamamatsu). After each sweep, vertical position of the lasers and imaging objective was changed by 5 or 8 μm until a full brain volume was acquired (3 volumes/second). For GCaMP6s/f imaging, a blue laser (488 nm) was used for excitation with a green 525/50 nm detection filter (Semrock). Red light delivered visual stimulus. For jRGECO1b imaging, a green laser (561 nm) was used for excitation with a red 630/92 nm filter for detection (Semrock). For two-color imaging, 488 nm and 561 nm lasers were used simultaneously. An image splitter (W-View Gemini, Hamamatsu) separated a green and a red component (with a 525/50 nm detection filter (Semrock) for green emission and a 645/75 nm detection filter (Chroma) for red emission); red and green images were recorded on opposite halves of the same camera chip. Blue light delivered stimulus (animals showed optomotor response to either blue or red light from the video projector).

Futility-induced passivity behavioral analysis

Futility-induced passivity was defined by the inter-swim-interval. Paralyzed fish in closed loop in our VR setup typically swam in discrete bouts, about once per second (1.2 ± 0.05 s, n = 74). When switched to open loop, after swimming for ~20 s, fish paused for ~20 s in the passive state. About 50% of fish showed this behavior at 6-7 d.p.f.; fish that did not become passive in the open loop protocol were not included in subsequent analyses (50%). The active/passive state switching created a bimodal distribution of inter-swim intervals (Figure S1A), according to which we chose 5 s as the threshold defining passive epochs. An active epoch was defined as a chain of swim bouts separated by intervals under 5 s with more than 5 s between the start of the first swim bout and the end of the last bout. The two types of intervals segregated epochs well (1.19 ± 0.047 s inter-swim-interval in active epochs versus 24.4 ± 2.5 s in passive epochs, n = 74, Figure S1B). The average length of active epochs was 36.1 ± 4.2 s, and the fish swam 29 ± 6 times (n = 74) during each epoch.

DMD-based optogenetic stimulation

To target specific populations of cells for optogenetic stimulation, we built two photostimulation modules using digital micromirror devices (DMD) from commercial projector displays (P-300, AAXA; Lightcrafter discovery kit, Texas Instruments; see Optical Pathway for Optogenetic Stimulation). One photostimulation module was integrated to a standard epifluorescence microscope, and the other was integrated to our light sheet microscope. The optical design of our photostimulation modules is described (Zhu et al., 2012a). Briefly, the DMD was illuminated by a blue laser (488 nm in setup 1; 473 nm in setup 2). Patterned light reflected off the DMD was spatially filtered with a pinhole to select the 0^{th} diffractive order, then the relayed image of the DMD was expanded and projected onto the sample plane of the microscope. We wrote C#, Python, and Arduino software to control the lasers and create spatial patterns for photostimulation (available upon request).

Parameters for optogenetic stimulation: For *Tg(dbh:KalTA4);Tg(UAS:CoChR-eGFP)* fish on setup 1, the excitation intensity was 0.17 mW / mm^2 and the stimulation duration was 3 s of 10 ms pulses at 10 Hz. For *Tg(gfap:opto-α1AR-eYFP)* fish on setup 1, the excitation intensity was 0.42 mW / mm^2; the stimulation duration was 10 s of continuous illumination. For *Tg(gfap:CoChR-eGFP)* fish on setup 2, the stimulation intensity ranged from 0.23 to 0.46 mW / mm^2; the stimulation duration was 3 s of 10 ms pulses at 10 Hz.

Two-photon ablation of cells

For plasma ablation of individual radial astrocytic cells, we used a two-photon laser (Coherent, Chameleon Ultra II). Cells were selected based on their location between rhombomere 2 and rhombomere 6, along the midline of the dorsal hindbrain, and a genetic marker in *Tg(gfap:H2B-GCaMP6f)* fish. Ablation was done with high laser power (930 nm, 500 mW, measured after the objective) directed to a single point on each cell with short exposure time (1 – 4 ms) and 300–400 ms between ablations to prevent thermal damage. After successful ablation, an image stack showed previously bright, round nuclei appeared dim, irregular or fragmented. Cells without this signature were selected again for the next round. Each fish underwent 3–5 rounds of ablation. The experiment started 30-60 min after the last ablation.

Noradrenergic neurons in LC and norepinephrine cluster of the medulla oblongata (NE-MO) were similarly ablated in *Tg(th-P2A-Gal4); Tg(UAS:GCaMP6s)* fish and serotonergic neurons in the dorsal raphe nucleus (DRN) were ablated in *Tg(elavl3:H2B-GCaMP6f)*. In this line, DRN cells were identified by their anatomical location. In control experiments, similar numbers of neurons labeled by *Tg(elavl3:H2B-GCaMP6f)* in nearby brain regions were ablated with the same protocol.

Forebrain lesioning

Fish were embedded in 2% agarose and anesthetized in external solution with tricaine (0.2 mg/mL) at 4 dpf. An incision was made at the top of the forebrain, and a glass pipette (inner diameter ~20 μm) was inserted until it touched the brain. Negative pressure was applied through a tube connected to the glass pipette, and the forebrain was removed by suction. Fish were released from agarose twenty minutes later and returned to the incubator. Behavior experiments were done at 6 dpf, when the forebrain was still largely missing. Siblings were used as controls. Control fish went through the same procedure except that their forebrain was left intact. During testing, two fish of similar body size, forebrain-intact and forebrain-removed, were put in the same rig and recorded simultaneously.

TRPV1-mediated activation of radial astrocytes

For TRPV1-mediated activation (Chen et al., 2016) of radial astrocytes, we injected *gfap:TRPV1-T2A-eGFP* plasmid into embryos from *Tg(gfap:jRGECO1b)* transgenic fish at the 1–2 cell stage. TRPV1 protein expressed sparsely in radial astrocytes. Fish were screened at 3 dpf: larvae with strong, sparse GFP expression in the hindbrain were the 'TRPV1 (+)' group; those without detectable GFP expression were the 'TRPV1(-)' group. Both groups were screened again based on expression of jRGECO1b, and subdivided into four groups: 'TRPV1(+) jRGECO1b(+)'; 'TRPV1(+) jRGECO1b(-)'; 'TRPV1(-) jRGECO1b(+)'; and 'TRPV1(-) jRGECO1b(-)'. All fish were tested behaviorally; jRGECO1b-positive fish were imaged in a light-sheet microscope. For all experiments, fish were recorded for at least 0.5 h, and then capsaicin (Sigma; 5 μM final concentration in system water) or saline was delivered into the recording chamber, and recording continued for 1 to 2 h.

Calcium responses and behavior were quantified in two 10-min windows: from 11 min to 1 min before capsaicin ('before' treatment) and from 10 to 20 min after capsaicin ('after' treatment).

IP_3 receptor blockade

To partially block the calcium concentration increase in radial astrocytes, we inhibited IP_3 receptor-dependent calcium release by loading the inhibitor Xestospongin C (Sigma) (Gafni et al., 1997) near astrocytic cell bodies. Glass pipettes were pulled on a micropipette puller (P-1000, Sutter Instruments), and broken on a microforge (MF900, Narashige), to get a 10 μm-wide tip. This sharp glass pipette was loaded with 5 μL of a mixture of Xestospongin C (100 μM, in external solution) and a fluorescent dye (Dextran, Texas Red, 0.5%, or Dextran, Fluorescein, 0.5%, Thermofisher) to visualize the ejection. The pipette was then inserted through the skin of a paralyzed *Tg(gfap:GCaMP6f)* fish and advanced to the hindbrain ventricle, near astrocytic somata. We first assessed how long the fish spent in a passive state while in open loop for 30 min. Then, pulses (20 psi, 30 ms, inter-pulse-interval 30 s, 10 pulses) were delivered using a pressure ejection system (Picosprizter III, Parker Hannifin). Fish were then switched to the closed-loop condition for ~20 min to allow the drug to take effect and then back to open loop to record the time spent in passivity.

Analysis of fluorescence imaging data

Calcium indicators

Multiple calcium indicators - GCaMP6f, GCaMP6s, H2B-GCaMP6f, jRGECO1b - were used for different purposes: single color imaging, dual-color simultaneous two-population imaging, imaging with optogenetic stimulation. For whole-brain imaging analysis, we tested both the calcium indicators (jRGECO1b and GCaMP6f) in both neurons and radial astrocytes, and found similar relationships between calcium responses and behavior with both indicators.

Summary of Calcium Indicators for Each Experiment

Cell type	Calcium indicator	Figures
Neurons	GCaMP6f	Figures 2A–2D, 2F, 2H, 2J–2M, 6A, and S2A–S2E
	H2B-GCaMP6f	Figures 4E, S1K, and S5F
	jRGECO1b	Figures 5R, S5G, and S5H; tested for consistency
Radial astrocytes	GCaMP6f	Figures 2D, 2G, 2H–2M, 4H, 5I (bottom), 7K, S2C–S2E, S4I, and S6G
	jRGECO1b	Figures 2A–2C, 4G, 5B, 5D, 5E, 5F, 5H, 5I (top), 6C, 6H, 6K, 6L, 6N, 7H, S2A, S2F, S5A, S5C, S5H, and S6F
	H2B-GCaMP6f	Figures 4B–4D, 4F, and 4G
Noradrenergic neurons	GCaMP6s	Figure 6B, 6C, 6E, 6F, 7B–7I, and S6H

Baseline normalization

For all functional imaging videos, baseline fluorescence was estimated by smoothing each pixel's time series with a sliding-window percentile filter that estimated the 20th percentile of the data in 5-min windows, after subtracting the camera baseline (~100). ΔF/F was then calculated for each pixel's time series (after subtracting camera baseline) by subtracting the baseline from the raw time

series and dividing this difference by the baseline plus an offset of 10, to prevent division by baseline values very close to 0. The addition of an offset to the denominator of the ΔF/F calculation underestimates true ΔF/F but reduces the rate of artifacts.

Extraction of cells from voxel data

We developed a data-processing pipeline to extract populations of cell bodies and neuropil, then cluster these cell segments (called 'cells') into functionally relevant components (cells with similar activity patterns and reproducible anatomical structure), and finally to align and compare cells and components at specific behavioral points and across fish.

For each fish, our analyses began with ANTs 2.1.0 rigid-body registration of all volumes to the average volume (Avants et al., 2010). Then we created an intensity-based brain mask and fully divided the brain into about 1000 spatially contiguous three-dimensional blocks, which overlapped slightly to capture cells on the borders.

We used the Spark cluster computing framework (Zaharia et al., 2010) to parallelize cell-detection across blocks. Our algorithm was based on constrained non-negative matrix factorization. For n voxels, t time points, and c cells, we factorized

$$V_{(n \times t)} \approx W_{(n \times c)} H_{(c \times t)} + X_{(n \times 1)} I_{(1 \times t)} \quad (1)$$

where V is the full spatiotemporal fluorescence matrix for each block, W and H are, respectively, the spatial location and time series of segmented cells, and X and I are a rank-1 spatiotemporal model of the background signal. We set the block size under the assumption that each block would contain 100 tightly packed 6 μm diameter spheres. Thus, we set the number of cells in each block to be 100, and then gradually reduced this number (through iterative multiplication by 0.95) until the system in Equation 1 was not rank-deficient and factorization converged.

We combined local intensity peaks and local correlation coefficients to initialize W (and used a constant value to initialize X); and approximately solved Equation 1 using alternating least-squares (Berry et al., 2007), with at least 10 iterations, and at most 100 iterations or until numerical convergence (defined as a change in the value of the residuals < 0.001).

We imposed spatial and temporal constraints to regularize this factorization, including mean-amplitude normalization of each cell; hard spatial constraints: retaining the largest connected segment within a static 12 μm diameter sphere (centered on a local-intensity peak); and soft sparseness constraints: a sparse projection of the spatial footprint for each cell using the algorithm of Hoyer (Hoyer, 2004), with sparseness,

$$\text{sparseness}(W_i) = \frac{\sqrt{n} - \sum_j |W_{ij}| \Big/ \sqrt{\sum_j |W_i|^2}}{\sqrt{n} - 1} \quad (2)$$

set to be at least equal to the spatial sparseness of a binary 6 μm diameter sphere (these constraints were not applied to the model of the background signal)

The resulting cell representation of whole-brain activity accurately reproduced the raw voxel time series and had increased signal-to-noise ratio due to demixing and denoising. Regions of neuropil and astrocytic processes were factorized similarly to cell bodies, also yielding small patches of voxels with consistent signals.

Clustering cells into components

We clustered segmented cells into functionally relevant components in two steps. First, we used non-negative matrix factorization to reduce the time series for all segmented cells in the brain into low-dimensional components. Specifically, for k cells, t time points, and $m = 60$ components, we factorized

$$H_{(k \times t)} \approx S_{(k \times m)} T_{(m \times t)} \quad (3)$$

where H are time series for all segmented cells in the brain, while S and T are the spatial and temporal low-dimensional components. These components need not be spatially localized, so we substituted local intensity-based initialization for nonnegative double SVD method (Boutsidis and Gallopoulos, 2008) and imposed no spatial constraints on this factorization.

Second, we detected components in this reduced representation. We deemed a component to be functionally relevant when it contained cells with similar activity patterns and showed robust and reproducible anatomical structure across fish (Figures 2D and 2E; Video S2). In contrast, noise components lacked clear spatial structure or were not reproducible across fish.

To evaluate reproducibility, we constructed an average brain template, independently for neurons and radial astrocytes, using the nonlinear registration tool antsMultivariateTemplateConstruction2 (Avants et al., 2010). We registered the spatial component of each fish to this template, and did semi-automated clustering across all components of all fish. We clustered spatial components by binning adjacent voxels of each component, computing the correlation coefficient between all components, thresholding the correlation matrix, and clustering the thresholded correlation matrix using the clique percolation method (Palla et al., 2005), an algorithm that can flexibly assign each component to more than one cluster or to no clusters. We manually fine-tuned this initial clustering by excluding components from clusters if the average spatial correlation of the component with the cluster was too low, and including the component if the average correlation of the component to all components within the cluster was sufficiently high. This step yielded 10-20 neuronal and astrocytic clusters. All components within each cluster were averaged, smoothed, and warped to individual fish space. Figures 2D and 2E shows the 10 group-average components with highest p values (see below), while Video S2 shows all group-average components created in this way for neurons and radial astrocytes.

To avoid misalignment of group-average components in individual fish, we used an additional nonnegative matrix factorization step, which aligned the components more tightly to each fish. Specifically, we refactorized H (Equation 3), with S initialized by and constrained to be within the binary mask of each group-average component. This added step allowed us to combine the consistency of components across multiple fish with the individual spatial variation of components within each fish. Finally, we averaged the activity of cells within the spatial mask of each component in individual fish, and compared this average across active and passive states.

Analysis of component and cell activity around passivity onset

We related neuronal and astrocytic component and cell dynamics to behavior by upsampling all calcium signals to 10 Hz, and registering them to passivity onset, and to the midpoints of bouts preceding this onset. As timings of individual bout sequences varied (relative to passivity onset) across trials, we registered bouts by averaging the relative times of bout sequences across trials and fish and linearly interpolating between individual-trial and average bout-sequence times.

This approach allowed us to study average activity of each component and cell relative to passivity onset (Figures 2F–2M; Video S3). We estimated the increase in calcium during and after passivity onset by comparing a sliding 1 s window of $(\Delta F/F)$ to the baseline, defined as the average over 10 to 5 s before passivity onset. We computed the significance of any increases in calcium by one-tailed Wilcoxon signed-rank test across trials. At this exploratory stage, we sought to identify candidate components and cells associated with passivity onset by computing $-\log_{10}(\text{p value})$, where p values from the Wilcoxon rank-sum were averaged between 1 s to 4 s after passivity onset.

We further analyzed the temporal profile of activity of neurons and radial astrocytes close to passivity onset at the single-cell level, by averaging activity of each segmented cell within a one-second window centered on the peak of each bout, and fitting an exponential function to the activity averaged over the last five bouts before passivity onset (Figure 6A). We interpreted the best-fit exponent of the cell as the rate at which single-cell fluorescence increased before the fish became passive.

Confocal microscopy

Confocal imaging was done using a Zeiss LSM 710, a Zeiss LSM 880 upright confocal, and a Zeiss LSM 800.

Single-cell radial astrocyte tracing

Tg(gfap:jRGECO1b) or *Tg(gad1b:RFP)* fish at 6 dpf were embedded dorsal side up in 2% agarose in a 35 mm Petri dish. The head was exposed by cutting away the agarose above the hindbrain. Fish were then imaged with a two-photon microscope at a wavelength of 1030 nm in the dorsal anterior hindbrain adjacent to the Lateral Medulla Oblongata (L-MO), at the level of rhombomeres 2-3, the approximate location of the rostral cluster of radial astrocytes. Single radial astrocytes were electroporated with 20% Texas Red Dextran or fluorescein Dextran, 3,000 MW, anionic, lysine fixable (Molecular Probes) as described (Koyama et al., 2011). For electroporation, we delivered 150 square pulses of 1 ms duration and 30 V at a frequency of 20 Hz using glass electrodes with an impedance of 240 MΩ. Then fish were released from agarose and transferred to the incubator. After overnight fixation in a 4% solution of paraformaldehyde in phosphate-buffered saline (PBS) pH 7.4 at 4°C, fish were dissected to expose the brain and imaged from the dorsal side on a Zeiss LSM 880 confocal microscope using a 25x objective. Confocal stacks were analyzed with FIJI (ImageJ).

In situ hybridization

Zebrafish larvae at 6 dpf were euthanized with an overdose of MS-222 (tricaine) and fixed overnight in 4% PFA-PBS, pH 7.4 at 4°C. Fish were dissected to expose the brain and processed for whole mount *in situ* hybridization (WISH) using the RNAScope technology by manufacturer protocol (Gross-Thebing et al., 2014). The adra1Bb custom probe was designed by the manufacturer and used on transgenic *Tg(gfap:GCaMP6f)* fish. Fish were then mounted in Vectashield (Vector Laboratories, Burlingame) and imaged on a Zeiss 800 upright confocal microscope with a 25x water immersion objective.

Immunohistochemistry with expansion microscopy

Tissue preparation

Fish brains were dissected out in PBS and fixed in 4% PFA-PBS, pH 7.4 overnight at 4°C, then rinsed well with PBS before antibody labeling.

Antibody staining

Brains were incubated in blocking buffer (10% goat serum, 0.8% Triton X-100 in PBS) overnight at 4°C. Brains were then incubated with primary antibodies chicken anti-GFP (Aves, GFP-1020) and rabbit anti-dsRed (Clontech, 632496) diluted 1:500 in blocking buffer, for 2 days at 4°C, followed by washing in wash buffer (0.3% Tween 20 in PBS) 5x 30 min at room temperature. Brains were incubated in fluorescent secondary antibodies goat anti-chicken Alexa Fluor 488 (Invitrogen, A11039) and goat anti-rabbit Alexa Fluor 594 (Invitrogen, A11037) diluted 1:500 in blocking buffer, for 2 days at 4°C, followed by washing in wash buffer 5x 30mins at room temperature. Brains were then washed and stored in PBS. All antibody staining steps included shaking.

Expansion

Expansion was done as described (Tillberg et al., 2016) (see also Freifeld et al., 2017). AcX was resuspended at 10mg/mL in anhydrous DMSO, aliquoted, and stored desiccated at –20°C for up to several months. AcX aliquots were diluted 1:100 in PBS to produce anchoring solution just before use. Specimens were incubated with at least 100-fold volume excess of anchoring solution, at room temperature overnight, protected from light, without shaking.

Gelation solution (8.6% (w/v) sodium acrylate, 2.5% (w/v) acrylamide, 0.15% (w/v) bisacrylamide, 2M sodium chloride, 1xPBS, 0.01% (w/v) 4HT, 0.2% (w/v) TEMED, and 0.2% (w/v) APS in milliQ water) was prepared as follows: all components except 4HT, TEMED, and APS were mixed to produce StockX, which was aliquoted and stored at −20°C for up to several months. Aliquots were thawed and chilled to 4°C, and then 4HT, TEMED, and APS were added from concentrated stocks (0.5% (w/v) 4HT, 10% (v/v) TEMED, 10% (w/v) APS) just before use. Specimens were incubated with at least 100-fold volume excess gelation solution 2x 10min at 4°C.

During the incubation in gelation solution, chambers were prepared by applying adhesive silicone gaskets (ThermoFisher Scientific, P24743) to plain glass slides and coating the glass bottom of each well with 1 μL poly-lysine coating solution (poly-lysine solution (Ted Pella 18026) with photo-flo (EMS 74257) added up to 0.2% (v/v)), leaving at least 5 min for poly-lysine coating solution to dry onto glass.

Following incubation in gelation solution, specimens were transferred to the middle of chambers, where they adhered to the poly-lysine treated surface, leaving at least 2 mm between each specimen and the chamber wall. Excess gelation solution was removed and replaced with 36 μL gelation solution for each 9 mm diameter chamber. Chambers were sealed with cover glass, which forms a seal with the silicone gasket under gentle pressure. Care was taken to avoid bubbles within 2 mm of specimens. Chambers were then held at 37°C for 2 h to gel and cure specimens. Chambers were moved to 37°C within 30 min of adding APS to the solution to prevent premature gelation.

After gelation, chambers were brought back to room temperature and disassembled. Top cover glass and silicone gaskets were carefully removed, leaving gels adhered to glass slides. Gels were trimmed using a razor blade to a right trapezoidal shape to aid in post-expansion orientation of the specimen. Several microliters of digestion buffer (0.5% (w/v) Triton X-100, 500 mM sodium chloride, 1 mM EDTA, 50 mM Tris pH 8) were applied around the edge of each gel to de-adhere them from the glass surface. Proteinase K (New England Biolabs, P8107S) was added 1:100 to digestion buffer to produce digestion solution. Gels were incubated in at least a 100-fold volume excess of digestion solution overnight, at room temperature, with shaking. Following digestion, gels were washed several times in PBS and kept at 4°C until further use.

Expansion and imaging

Gels were expanded by washing in water and imaged on a Zeiss Z1 light sheet microscope with standard settings (Figure 3) or a Zeiss LSM 880 confocal microscope (Figure S3). Adjacent volumes were stitched using the Zeiss ZEN software. In Figures 3 and S3, stitching artifacts arising from non-ideal software stitching are indicated with arrowheads and dashed lines.

Materials Used Specifically for Expansion Microscopy

Name	Formal name	Supplier	Cat #
AcX	Acryloyl-X, SE, 6-((acryloyl)amino) hexanoic Acid, Succinimidyl Ester	ThermoFisher Scientific	A20770
Sodium acrylate	Sodium acrylate	Sigma	408220
Acrylamide	Acrylamide	Sigma	A9099
Bisacrylamide	N,N′- Methylenebisacrylamide	Sigma	M7279
4HT	4-Hydroxy-TEMPO	Sigma	176141
TEMED	N,N,N′,N′- Tetramethylethylenediamine	Sigma	T7024
APS	Ammonium persulfate	Sigma	A3678

RNA sequencing

Cell isolation, library preparation, and sequencing

Neurons and radial astrocytes were isolated using methods of Hempel et al. (2007) with minor modifications. Fish were euthanized with 1:30 dilution MS-222/Tricaine in external solution, then placed on ice. Brains were dissected in 1:30 dilution of MS-222/Tricaine in external solution, then digested with Liberase-DH (1 mg/mL; Roche) in external solution for about 1 h. Digested brains were washed three times in external solution with 1:30 dilution of MS-222/Tricaine. Digested brains were triturated as described (Hempel et al., 2007) in external solution containing Tricaine and 2% fetal bovine serum. Cells were isolated by hand. About 300 cells were collected for each sample and lysed in 50 μl PicoPure extraction buffer. RNA was extracted and libraries were prepared as described (Cembrowski et al., 2016). Briefly, cDNA was prepared from DNase-treated RNA using Ovation RNA-seq v2 kit (NuGEN). Barcoded libraries were prepared with Ovation Rapid library kit (NuGEN) and sequenced on a HiSeq 2500 to a depth of about 40 M reads per sample with single-end 100 bp reads.

Gene expression estimation

Sequencing adapters were trimmed from the reads using cutadapt (https://doi.org/10.14806/ej.17.1.200). Trimmed reads were aligned to danRer10 Refgene transcriptome (UCSC). Gene expression estimates were reported as transcripts per million.

Optical Pathway for Optogenetic Stimulation

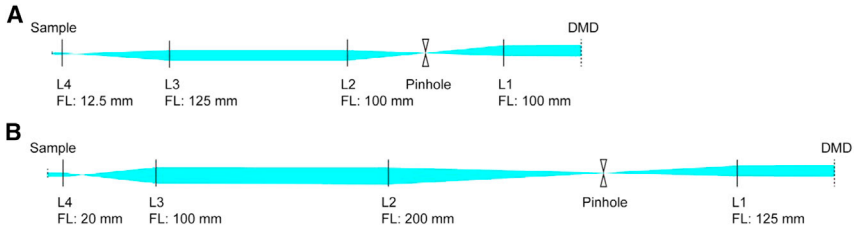

Optics in the two DMD photostimulation modules. The chief difference between these designs is demagnification of DMD image at focal plane of L4 (objective lens).

(A) Setup 1, photostimulation module in light sheet microscope. This module was used for all experiments that combined optogenetics with calcium imaging. As this module is designed for one photostimulation wavelength, lenses F1-F3 in panel A are singlets (Thorlabs). Final demagnification of DMD chip is 0.1X.

(B) Setup 2, Photostimulation module used in epifluorescence microscope. This module was used for all optogenetic experiments without calcium imaging. As this module is designed for two photostimulation wavelengths, lenses F1 - F3 in Panel B are achromatic doublets (Thorlabs). The final demagnification is 0.32X.

DATA AND CODE AVAILABILITY

The code for cell segmentation and component detection is available at https://github.com/mikarubi/segmentation.

Cell

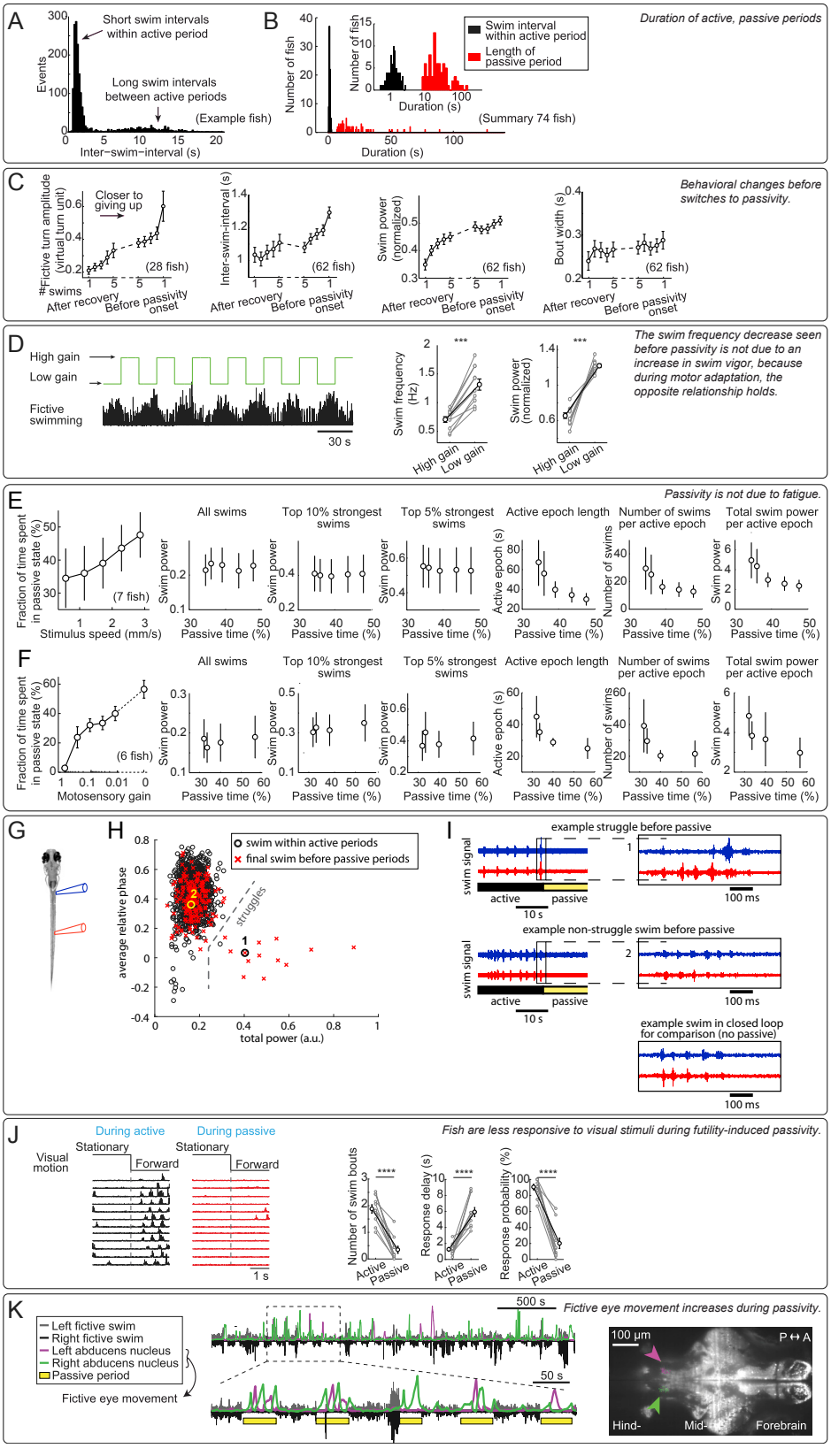

(legend on next page)

Figure S1. Higher-Order Behavioral Effects of Futility-Induced Passivity, Related to Figure 1

(A and B) Distribution of inter-swim intervals in open-loop. Intervals followed a bimodal distribution: short swim intervals occurred within the active period when fish swam once every 1-2 s, and long swim intervals occurred between active periods when the fish stopped swimming (defined as the 'passive period'). (A) Distribution of all inter-swim-intervals from an example fish. (B) Distribution of average inter-swim-intervals during classified active periods (black bars), and average duration of passive periods (red bars) across fish.

(C) Over the course of an active period in open-loop, the animals: 1. made larger turns, and turning amplitude was largest just before passivity onset; 2. swam less frequently, and the longest interval between swims happened just before passivity onset; 3. swam more vigorously, and swimming was on average strongest just before passivity onset; 4. but the duration (width) of swim bouts was not strongly modulated. Error bars, SEM.

(D) Decrease in swim frequency (seen before passivity in C) is not due to an increase in swim power, control for Figure 1I. (*Left*) Motor adaptation assay; low motosensory gain in a closed-loop environment led to more powerful swimming. (*Right*) During low motosensory gain, swim frequency and swim power were both elevated compared to during high motosensory gain. Therefore, the decrease in swim frequency observed as the animal approaches passivity (Figure 1I) was not simply due to a concurrent increase in swim power. (Two-tailed paired t test, ***$p < 0.001$, $p = 8.9 \times 10^{-6}$ for swim frequency, $p = 2.7 \times 10^{-6}$ for normalized swim power. Error bars, SEM)

(E and F) Effects of stimulus velocity and motosensory gain on futility-induced passivity imply that passivity was unlikely to be caused by fatigue. More passivity was caused by (E) faster forward-moving visual stimulus in open loop, or (F) lower motosensory gain in closed loop. Under those conditions, increased occurrence of passivity was not due to more vigorous or more frequent swimming because: similar swim power of individual swims was observed for different velocities or gains, as well as of the top 10% strongest swims and the top 5% strongest swims. On the contrary, more passivity can be associated with smaller amounts of total swim output: shorter active periods, fewer swim attempts, and less total swim power. Together, these results imply that passivity was not caused by fatigue. Error bars, SEM.

(G–I) During transitions from active periods to passive periods, fish occasionally struggle. (G) Experimental setup showing placement of an electrode pair, recording electrical signals from the same side but different segments of the tail (Liao and Fetcho, 2008). (H) Struggles can be identified by the relative phase difference between anterior and posterior electrodes, and power per burst. Final swims before passivity can be non-struggle swims or struggles. On average 13 ± 9% of switches are preceded by a struggle (identified by burst power, n = 5 fish, mean ± SEM). (I) Example of switches preceded by a struggle (top), non-struggle swim (middle), and for comparison, closed-loop swimming (bottom).

(J) Fish were less responsive to visual stimuli during the passive periods. In an assay where, first, passivity was elicited by the usual paradigm, then a static stimulus was presented (2 s), and then pulse of visual motion was presented (2 s), the animals responded far less to the motion pulse if they were in the passive behavioral state. (Two-tailed paired t test, ****$p < 0.0001$, $p = 2.6 \times 10^{-6}$ for swim bout number change, $p = 3.8 \times 10^{-5}$ for response delay, $p = 4.2 \times 10^{-7}$ for response probability. Error bars, SEM) Same data as in Figure 1K.

(K) During the passive periods, calcium activity was seen in neurons in the abducens nucleus (arrows) in animals expressing nuclear-localized GCaMP6f (*Tg(elavl3:H2B-GCaMP6f)*) imaged with a light-sheet microscope. Neurons in the abducens nucleus are known to drive eye movement. Thus, increased activity in this area, alternating between left and right, implies that animals were attempting to move their eyes during the passive periods.

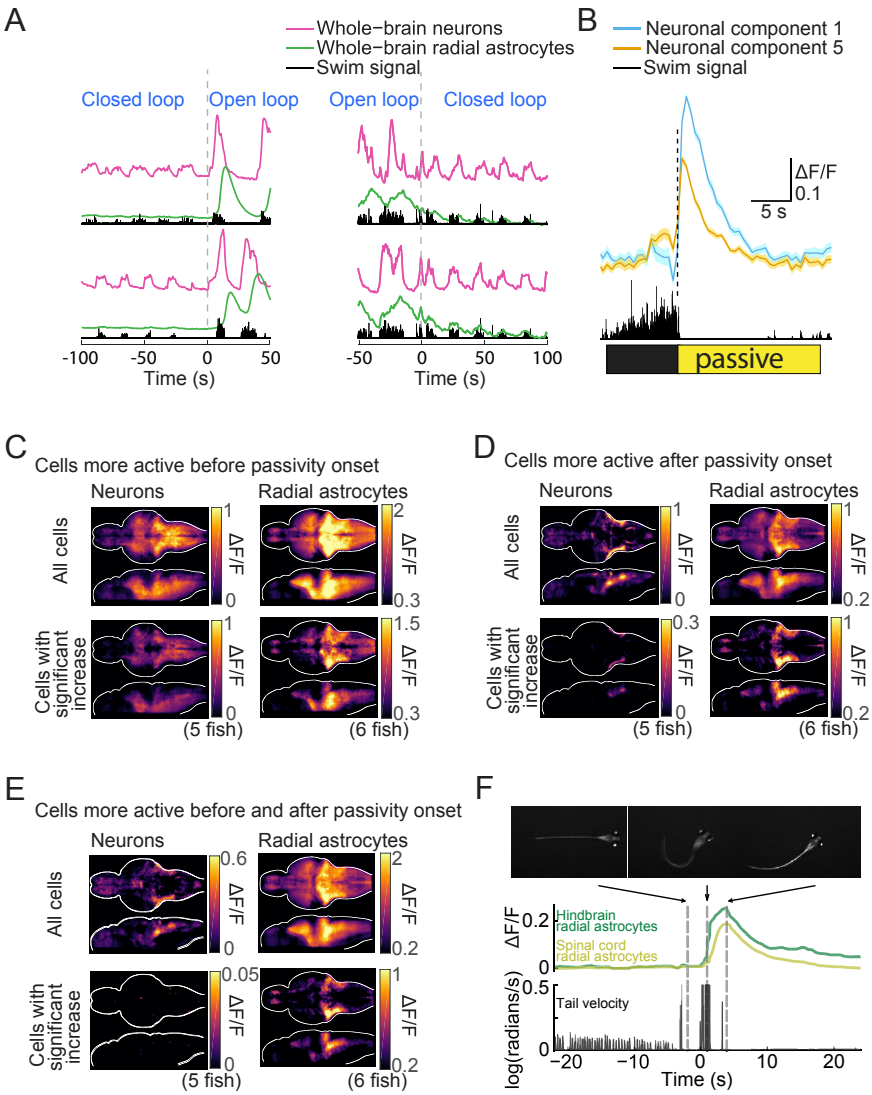

Figure S2. Whole-Brain Activity Elevation before and after Passivity Onset in Both Paralyzed and Non-paralyzed Fish and Passivity in Non-paralyzed Fish, Related to Figure 2

(A) Neuronal and astrocytic activity near the time of open-loop onset (left), and closed-loop onset (right). Signals are averaged across all the neurons or all the radial astrocytes in the brain, and two switches from each type are shown (top and bottom). Neurons showed stronger activity fluctuations during open-loop than during closed-loop, but showed clear activity patterns in both scenarios. In contrast, astrocytic activity fluctuations (calcium) were small before open-loop, but increased before and during passivity. Signals are z-scored.

(B) Average activity of neuronal component 1 and component 5, from the same fish in Figure 2H, triggered by passivity onset. Each trace is the average of 42 switches from active to passive states. Shading represents SEM.

(C–E) Whole-brain neuronal and astrocytic maps for cells showing activity elevation in windows before, after, or both before and after passivity onset (average over 5 fish for neuronal imaging, 6 for astrocytic imaging). Average ΔF/F signals from cells statistically increasing their activity relative to baseline (Methods),

(C) before passivity onset (−1 to 0 s).

(D) after passivity onset (+1 to 4 s).

(E) both before and after passivity onset (−1 to 0 s and +1 to 4 s).

For each panel, top rows show average activity from all cells, and bottom rows show average activity only from cells with significant activity elevation.

(F) A zebrafish, expressing GCaMP6f in radial astrocytes, was placed in agarose. The agarose was slowly coagulating, but never fully prevented tail motion. The fish attempted to swim and the viscous agarose prevented the movement, qualitatively mimicking a reduction in motosensory gain. The animals displayed similar passivity as in the virtual reality assay. Calcium levels followed a similar pattern as was seen in futility-induced passivity in virtual reality. Calcium activity also increased in the spinal cord, but with a delay.

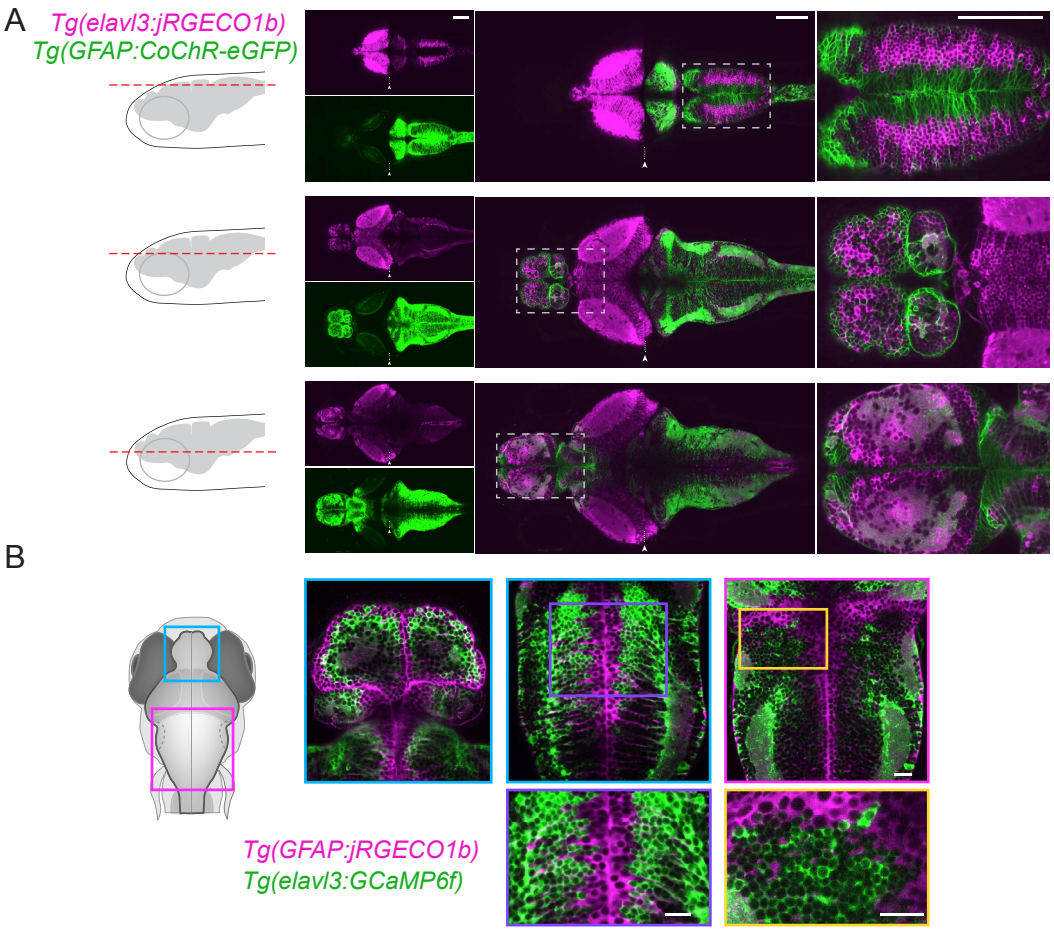

(legend on next page)

Figure S3. Anatomical and Electrophysiological Properties of Radial Astrocytes Projecting to the L-MO, Related to Figure 3

(A) Distinct expression patterns of CoChR-eGFP driven by the *gfap* promoter and jRGECO1b driven by the *elavl3* promoter suggests that the *gfap*-driven expression was largely restricted to radial astrocytes. Three columns represent three sections arranged from dorsal to ventral across the brain, indicated by the horizontal dashed lines in the schematic at the top of each column. *Row 1*, separated channels for CoChR-eGFP and jRGECO1b (the green channel was overexposed in order to visualize the low-level fluorescence in the tectum); *Row 2*, merged view of those two channels; *Row 3*, zoomed-in view of the region outlined by dashed lines in *Row 2*. Arrowheads indicate microscopy software stitching artifacts. Scale bars, 100 μm.

(B) Distinct expression patterns of jRGECO1b driven by the *gfap* promoter and GCaMP6f driven by the *elavl3* promoter, the combination being used for simultaneous imaging of radial astrocytes and neurons. Scale bars, 20 μm.

(C) Schematic side view of the fish brain showing the position of the panel (D) and the cross sections in (E) and (F).

(D) Side view of a section of the hindbrain showing astrocytic cell bodies and processes (white arrow) and the lateral hindbrain neuropil (yellow arrow). Scale bars, 100 μm.

(E) Cross section from a level of the hindbrain that contains the lateral hindbrain (L-MO) (the cyan box inset contains the L-MO). Scale bars, 100 μm.

(F) Cross section at the level of the cerebellum showing the midbrain-hindbrain border (MHB) (arrow). *Top-Left,* Astrocytic cells are shown in green; DAPI staining labels nuclei of all cells (neurons and radial astrocytes). *Bottom-Left,* astrocytic cells only. *Purple box inset*, astrocytic cell bodies (white arrow) can be seen along the dorsal midline and the MHB. Neurons are dark without the GFAP label (yellow arrow). *Cyan box inset,* long astrocytic processes extend dorso-ventrally and terminate in the lateral and ventral gliopil. Scale bars, 100 μm.

(G) Patch-clamp recording of a GCaMP6f-positive cell from a *Tg(gfap:GCaMP6f)* fish shows electrophysiological properties of radial astrocytes: (1) a linear voltage change in response to injected current, (2) more negative resting membrane potential than typical neuronal membrane (−84 mV), consistent with known recordings of radial astrocytes in zebrafish (Li et al., 2015). Error bars, SEM.

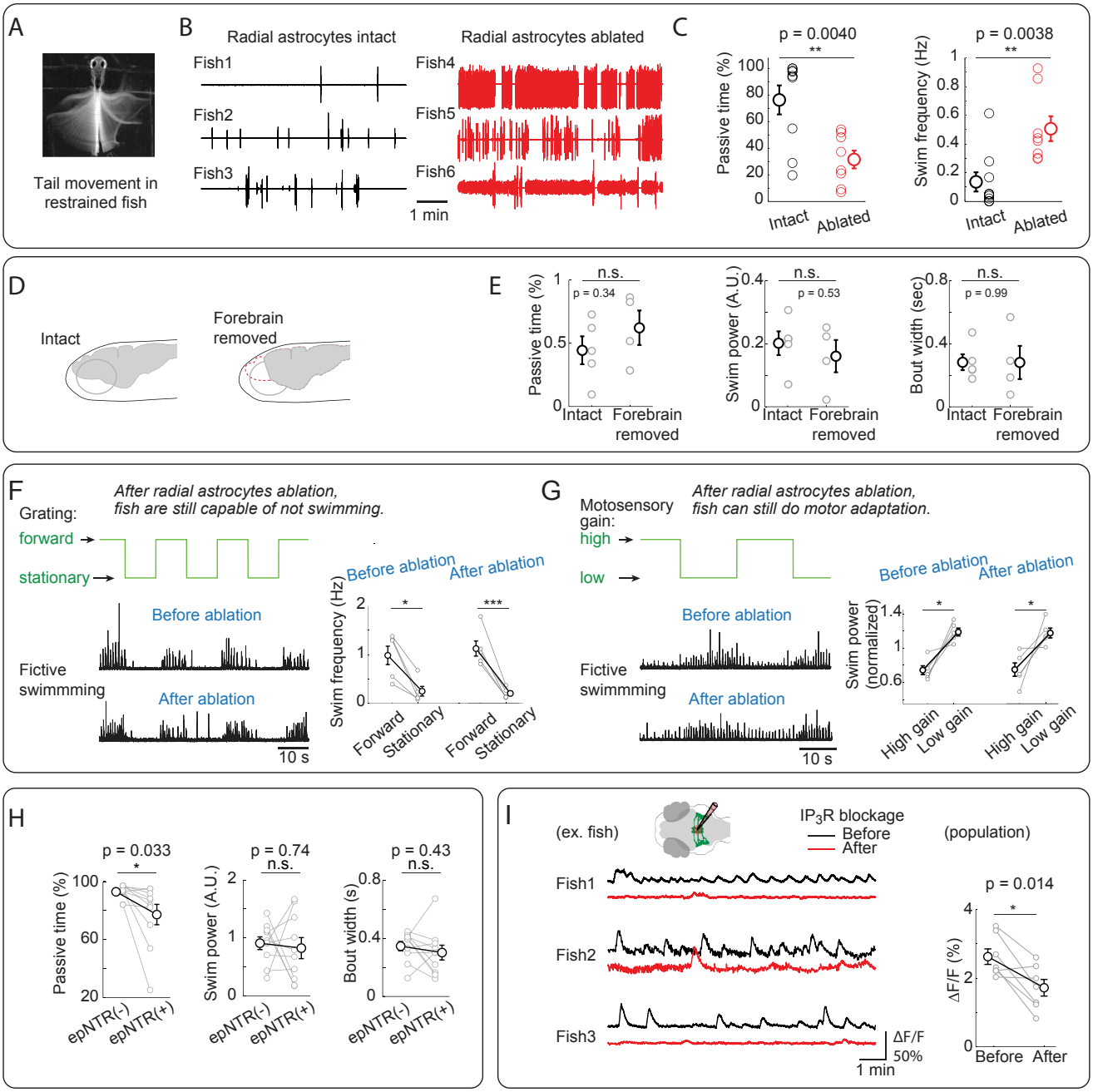

Figure S4. Details of Radial Astrocytes Inactivation, Related to Figure 4

(A–C) Astrocytic ablation in non-paralyzed zebrafish also reduces futility-induced passivity. (A) Fish were embedded in agarose, which was cut away around the tail, eyes and mouth. A time lapse image is shown during vigorous tail movement. (B) Non-paralyzed fish performed futility-induced passivity when head-embedded in agarose. With radial astrocytes intact, swimming occurred rarely. This may be due to the lack of visual feedback during tail movement, as well as the perception of pressure on the upper section of the trunk and head during tail movement. After laser ablation of radial astrocytes, the animals swam much more often. (C) Population data, showing a decrease in time spent passive and an increase in average swim frequency after astrocytic ablation (two-tailed non-paired t test, $^{**}p < 0.01$, $p = 0.0040$ for passive time, $p = 0.0038$ for swim frequency). Error bars, SEM.

(D and E) Removing the forebrain doesn't decrease passivity during open-loop. Removing the forebrain (D, Methods) did not reduce passivity during open-loop (E), showing that non-specific brain damage, of neurons or radial astrocytes, was not the reason for the reduction in passivity. Fictive swimming behavior was similar between the forebrain intact and forebrain-removed siblings (two-tailed non-paired t test). Error bars, SEM.

(F and G) Animals with radial astrocytes ablated can still perform motor adaptation and are still capable of not swimming. (F) When presented with forward visual motion alternating with a stationary stimulus, animals swam little during the stationary periods, both before and after astrocytic ablation, showing that ablation of radial astrocytes does not affect the ability of the animals to stop swimming. (G) Animals performed motor adaptation in a closed-loop environment, before and

(legend continued on next page)

after astrocytic ablation, showing that ablation of radial astrocytes does not affect the ability of the animals to modulate swim vigor. (Two-tailed paired t test, *$p < 0.05$, ***$p < 0.001$, $p = 0.014$ for before ablation, $p = 9.8 \times 10^{-4}$ for after ablation in (F); $p = 0.013$ for before ablation, $p = 0.042$ for after ablation in (G)). Error bars, SEM.

(H) Chemogenetic injury to radial astrocytes leads to a decrease in passive periods but leaves other swim behavior unchanged. The addition of a low concentration of the prodrug metronidazole (10 mM, incubation 8 h) (Tabor et al., 2014) caused intracellular damage to radial astrocytes in *Tg(gfap:epNTR)* fish that expressed nitroreductase in astrocytic cells. (Two-tailed paired t test, *$p < 0.05$, $p = 0.033$ for passive time, $p = 0.74$ for swim power, $p = 0.43$ for bout width). Error bars, SEM.

(I) Blocking inositol 1,4,5-trisphosphate receptor (IP_3R) reduces calcium activity in L-MO astrocytic cells during open loop. *Left,* calcium signals in astrocytic processes in the L-MO before (black) and after (red) injection of the IP_3R inhibitor, showing that calcium signals were reduced by the blockade of IP_3R. *Right,* population data showing that the reduction in calcium signal was consistent across animals. (Two-tailed paired t test, *$p < 0.05$, $p = 0.014$). Error bars, SEM.

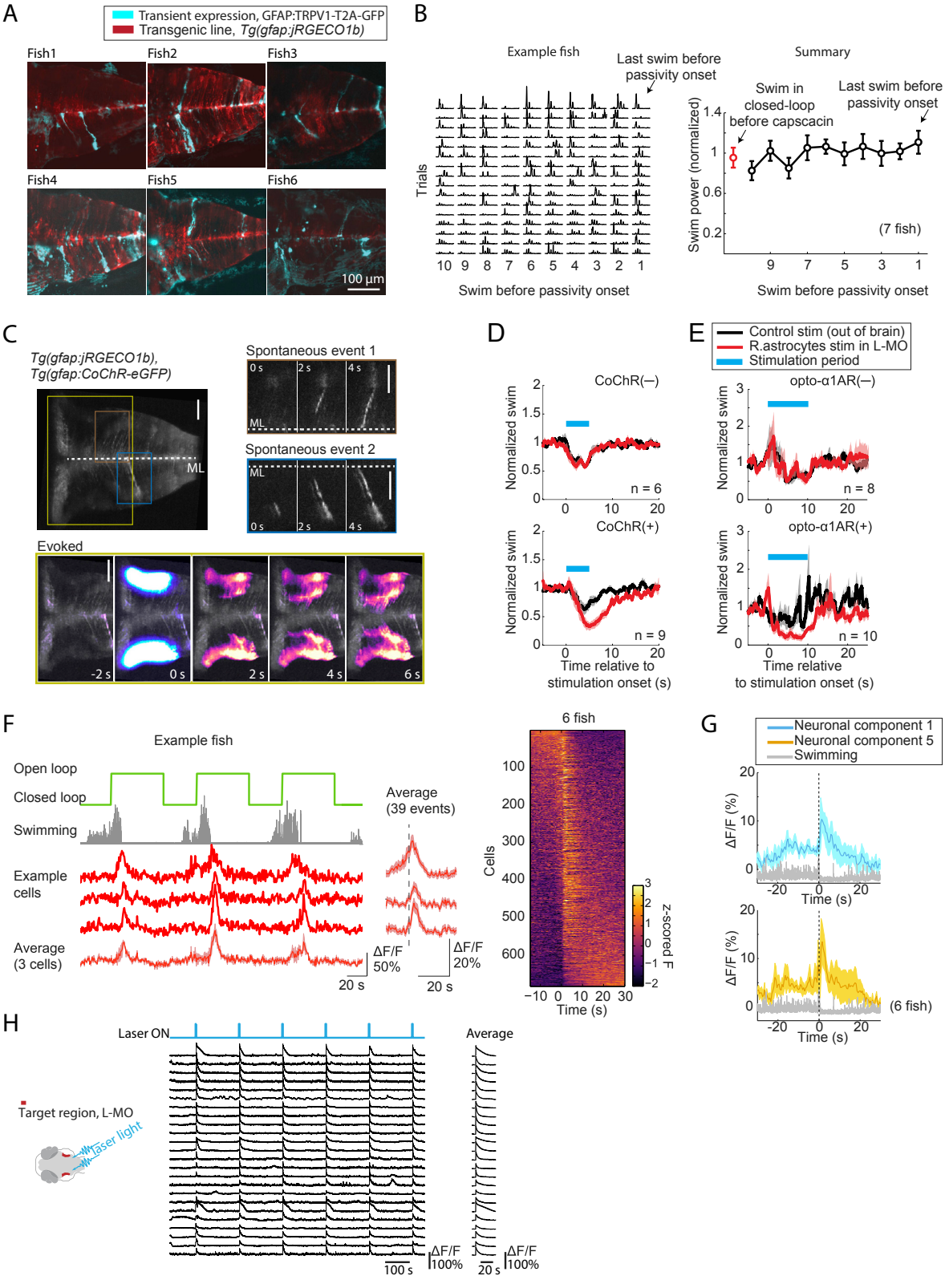

(legend on next page)

Figure S5. Details of Chemogenetic and Optogenetic Activation of Radial Astrocytes, Related to Figure 5

(A) Sparseness of expression of TRPV1. Maximum intensity projections along the dorsal-ventral axis of hindbrain volumes acquired with a light sheet microscope show that TRPV1 (Chen et al., 2016) channels (introduced into the fish by injection of a *gfap:TRPV1-T2A-GFP*, plasmid into *Tg(gfap:jRGECO1b)* transgenic embryos) were sparsely expressed in radial astrocytes. Expression was seen in about 10-50 astrocytic cells per animal, but opening of the TRPV1 channel with capsaicin activated a much wider population of glial cells (at least hundreds, likely through communication between radial astrocytes). Expressing cells showed the morphology of hindbrain radial astrocytes, with somata along the midline and processes extending laterally and then ramifying. (Note, the images show some contamination from skin autofluorescence. Also note, the jRGECO1b expression was more patchy than usual, likely because the co-injected *Tol2* transposase removed the *jRGECO1b* transgene from the genome of some cells.)

(B) Artificially activating radial astrocytes induces passivity without increasing swim vigor, consistent with a role for radial astrocytes in specifically suppressing swimming. Passivity was caused in closed-loop by applying capsaicin to fish that expressed TRPV1 (Chen et al., 2016) in radial astrocytes. In the swim bouts just prior to TRPV1-mediated passivity, swim vigor did not increase as it did during futility-induced passivity (Figure S1C) – rather, swim vigor stayed at a similar level as swims in closed-loop without capsaicin, showing that radial astrocytes caused passivity independently of increases in swim vigor. In example fish (left panel), each row represents the final 10 swims of an active period before the fish switched to a passive state. Error bars, SEM.

(C) Optogenetic stimulation during functional imaging of radial astrocytes shows that exciting these cells can cause spatially propagating calcium activity. Top row: after optogenetic excitation of astrocytic processes in the L-MO, a wave of calcium can be seen propagating from the site of excitation to the astrocytic cell bodies located along the midline. The time course of evoked activity resembles spontaneous activity of single astrocytic cells (top right), which suggests that optogenetic stimulation is sufficient to drive an endogenous calcium-dependent excitatory pathway in radial astrocytes. Scale bars, 20 μm.

(D and E) Optogenetic stimulation of L-MO astrocytic processes suppresses swimming. (D) *Top:* CoChR-negative controls showed no difference in behavior when the L-MO was stimulated or light was targeted outside of the brain (targeted to the ear, chosen because it is very close to the L-MO but outside the brain). A small response to the blue light was present if either the L-MO or the ear was targeted. *Bottom:* The same experiment in animals expressing CoChR in radial astrocytes showed a difference in behavior, with L-MO stimulation leading to a prolonged suppression of swimming. In total 30 pulses with a width of 10 ms and inter-pulse-interval of 90 ms were delivered for each stimulation (Methods). Shading represents SEM (E) Stimulation in Opto-α1-AR expressing animals similarly showed a suppression of swimming. A continuous 10 s of light stimulation was delivered for each stimulation (Methods). Shading represents SEM.

(F) GABAergic neurons in L-MO activated during switches to passivity. Left, fish switching to the passive state after entering open-loop, with activity increases in GABAergic neurons in L-MO at the time of switches. Right, summary of all GABAergic neurons in L-MO from 6 fish. Cells are ordered by the center of mass along the time axis. Shading represents SEM.

(G) Capsaicin activation of astrocytic calcium causes an increase in neuronal activity in L-MO neurons, consistent with the activation of GABAergic neurons in L-MO after astrocytic stimulation (Figure 5R). Shading represent SEM.

(H) Optogenetically stimulating radial astrocytes causes increases in neuronal activity in L-MO neurons. Shading represents SEM.

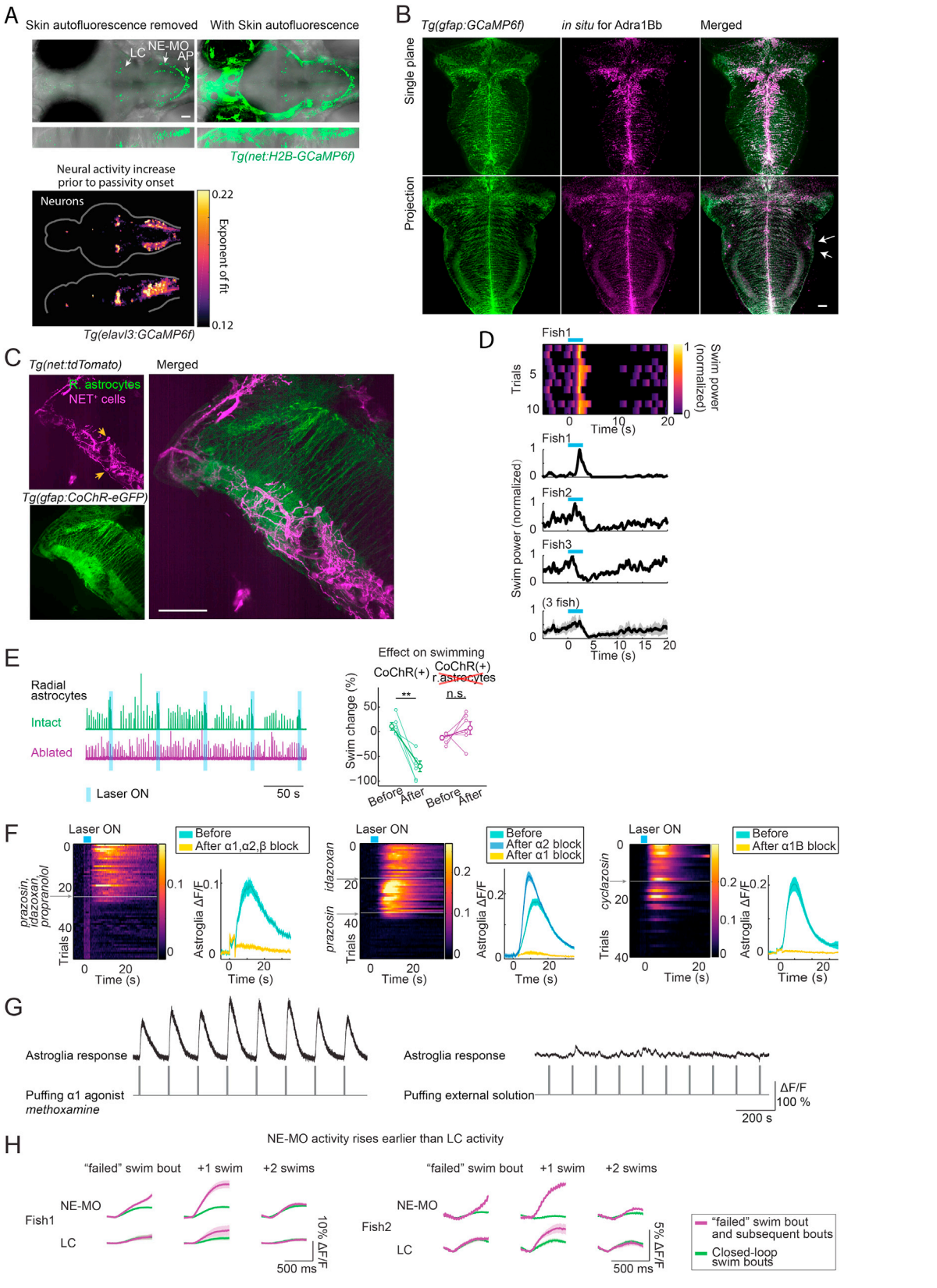

(legend on next page)

Figure S6. Calcium Signals in Noradrenergic Neurons Increase before Switches to Passivity, Noradrenergic Receptors Are Highly Expressed and Co-localized with Radial Astrocytes in the Lateral Hindbrain, Activation of Noradrenergic Neurons Can Elicit a Transient Increase in Motor Vigor, and Coding for Swim Failures in Different NE Nuclei, Related to Figures 6 and 7

(A) *Top:* The nuclei of noradrenergic (NE) neurons (Farrar et al., 2018) are labeled in *Tg(net:H2B-GCaMP6f)* fish. *Bottom:* The neurons which increase their activity fastest prior to passivity onset overlap with the regions where the somata of noradrenergic cells, including the locus coeruleus (LC) and the NE cluster of the medulla oblongata (NE-MO), are located. Imaged line in the bottom panel is *Tg(elavl3:GCaMP6f)*. For easier visualization of noradrenergic cells, skin auto-fluorescence was removed manually in the top-left panel.

(B) Adrenergic receptor 1Bb expression visualized through *in situ* hybridization. The lateral hindbrain (L-MO) showed high levels of adra1Bb receptor expression (arrows). The receptors can also be seen to line the astrocytic processes that run medial-lateral, consistent with RNA-seq results (see Table S2). The projection is over a 40 μm thick section.

(C) Maximum intensity projection over 50 μm at the level of the L-MO of a *Tg(gfap:CoChR-eGFP); Tg(net:tdTomato)* fish that was expanded 4× through expansion microscopy to show a dense network of noradrenergic fibers expressing the norepinephrine transporter (NET) intertwined with glial processes in the L-MO. The section also shows the cell bodies of noradrenergic neurons (yellow arrows) located at the along the length of the medulla showing that indeed, noradrenergic neurons of the medulla oblongata (NE-MO) project to the L-MO.

(D) Photostimulating NE-MO can briefly potentiate swimming. In closed-loop, optogenetically stimulating NE-MO first increased swim vigor before it suppressed swimming. *Top*, single trials from an example fish. *Bottom,* mean swim power change from 3 example fish and the average from these 3 fish. Shaded region represents SEM.

(E) Photostimulating NE-MO no longer suppresses swimming after ablation of radial astrocytes in L-MO.

(F) Blocking α1 adrenergic receptors, but not α2 adrenergic receptors, abolishes the activation of radial astrocytes in L-MO by NE-MO stimulation. Optogenetic stimulation of NE-MO activates radial astrocytes in L-MO, and this activation was abolished by either adding a mixture of antagonists targeting multiple subtypes of adrenergic receptors (*left*, prazosin for α1, idazoxan for α2, propranolol for β), by an antagonist of α1 adrenergic receptors alone (*middle*), or by an antagonist of α1B adrenergic receptors alone (*right*), but not by an antagonist of α2 adrenergic receptors (*middle*). Shading represents SEM.

(G) Puffing methoxamine, an agonist of the α1 adrenergic receptor, triggered calcium responses in radial astrocytes in L-MO (*left*). Puffing external solution didn't trigger a response (*right*).

(H) Calcium activity in the NE-MO represents swim failures (Figure 7A). Calcium activity in the LC also represents swim failures, but only on the subsequent swim bout; this response may be downstream of the response in the NE-MO. The signals were aligned by subtracting the fluorescence right before the swim onset. Shading represents SEM.

Scale bar in (A-C): 50 μm.